

The VLT LBG Redshift Survey^{*} II: Interactions between galaxies and the IGM at $z \sim 3$

N. H. M. Crighton^{1†}, R. Bielby^{1,2}, T. Shanks¹, L. Infante³, C. G. Bornancini^{4,5}, N. Bouché⁶, D. G. Lambas^{4,5}, J. D. Lowenthal⁷, D. Minniti^{3,8}, S. L. Morris¹, N. Padilla³, C. Péroux⁹, P. Petitjean², T. Theuns^{10,11}, P. Tummuangpak¹, P. M. Weilbacher¹², L. Wisotzki¹² & G. Worseck¹³

¹Department of Physics, University of Durham, South Road, Durham DH1 3LE, UK

²Institut d'Astrophysique de Paris, UMR7095 CNRS, Université Pierre et Marie Curie, 98 bis Bld Arago, 75014, Paris, France

³Departamento de Astronomía y Astrofísica, Ponticia Universidad Católica de Chile, Casilla 306, Santiago 22, Chile

⁴Instituto de Astronomía Teórica y Experimental, IATE, Observatorio Astronómico, Universidad Nacional de Córdoba, Laprida 854, X5000BGR, Córdoba, Argentina.

⁵Consejo Nacional de Investigaciones Científicas y Técnicas, Avenida Rivadavia 1917, C1033AAJ, Buenos Aires, Argentina.

⁶University of Santa Barbara, Broida, Santa Barbara, 93106, USA

⁷Department of Astronomy, Smith College, Northampton, MA 01063, USA

⁸Vatican Observatory, V00120 Vatican City State, Italy

⁹Laboratoire d'Astrophysique de Marseille, OAMP, Université Aix-Marseille & CNRS, 13388 Marseille cedex 13, France

¹⁰Institute of Computational Cosmology, Department of Physics, University of Durham, South Road, Durham DH1 3LE, UK

¹¹Universiteit Antwerpen, Campus Groenenborger, Groenenborgerlaan 171, B-2020 Antwerpen, Belgium

¹²Astrophysikalisches Institut Potsdam, An der Sternwarte 16, D-14482 Potsdam, Germany

¹³Dept of Astronomy and Astrophysics, UCO/Lick Observatory, University of California, 1156 High Street, Santa Cruz, CA 95064

Accepted X December 15. Received X December 14; in original form X October 11

ABSTRACT

We have measured redshifts for 243 $z \approx 3$ quasars in nine VLT VIMOS LBG redshift survey areas, each of which is centred on a known bright quasar. Using spectra of these quasars, we measure the cross-correlation between neutral hydrogen gas causing the Ly α forest and 1020 Lyman-break galaxies at $z \approx 3$. We find an increase in neutral hydrogen absorption within $\approx 5 h^{-1}$ Mpc of a galaxy in agreement with the results of Adelberger et al. (2003, 2005). The Ly α -LBG cross-correlation can be described by a power-law on scales larger than $3 h^{-1}$ Mpc. When galaxy velocity dispersions are taken into account our results at smaller scales ($< 2 h^{-1}$ Mpc) are also in good agreement with the results of Adelberger et al. (2005). There is little immediate indication of a region with a transmission spike above the mean IGM value which might indicate the presence of star-formation feedback. To measure the galaxy velocity dispersions, which include both intrinsic LBG velocity dispersion and redshift errors, we have used the LBG-LBG redshift space distortion measurements of Bielby et al. (2010). We find that the redshift-space transmission spike implied in the results of Adelberger et al. (2003) is too narrow to be physical in the presence of the likely LBG velocity dispersion and is likely to be a statistical fluke. Nevertheless, neither our nor previous data can rule out the presence of a narrow, real-space transmission spike, given the evidence of the increased Ly α absorption surrounding LBGs which can mask the spike's presence when convolved with a realistic LBG velocity dispersion. Finally, we identify 176 C IV systems in the quasar spectra and find an LBG-C IV correlation strength on scales of $10 h^{-1}$ Mpc consistent with the relation measured at \approx Mpc scales.

Key words: intergalactic medium, galaxies: high-redshift

1 INTRODUCTION

The interaction between galaxies and the surrounding intergalactic medium (IGM) is a crucial component of galaxy formation. The majority of baryons at $z \sim 3$ reside in the intergalactic medium (e.g. Petitjean et al. 1993; Miralda-Escudé et al. 1996; Schaye 2001). It is from this reservoir of gas that galaxies draw fuel for star formation.

Star formation and active galactic nuclei (AGN) are in turn believed to have a significant effect on the IGM. Winds generated by supernovae in starburst events are observed to eject the interstellar medium (ISM) with velocities of hundreds of km s^{-1} with respect to the host galaxy (Veilleux et al. 2005) and are believed to be able to influence the IGM more than 100 kpc away from the galaxy (e.g. Wilman et al., 2005). Jets from AGN have been observed to extend hundreds of kpc from their host galaxy. There is considerable evidence for winds being commonplace in star-forming galaxies at $z \sim 3$. The spectra of Lyman break galaxies (LBGs, so-called because they are selected by their drop in flux at rest-frame 912 Å) show a systematic velocity offset between their Ly α emission features, absorption features (such as C IV, Si IV), and their nebular emission features (such as H α). Absorption features that are associated with the galaxy's ISM are blue-shifted by 200–300 km s^{-1} with respect to the true position of the galaxy, assumed to be given by the nebular emission features (Pettini et al. 2001). This blueshift is interpreted as an outflow velocity: the metal-enriched ISM gas is being pushed out of the galaxy towards the surrounding IGM. Metal enriched gas has also been observed up to ~ 80 kpc around $z \approx 2.3$ LBGs, consistent with models for accelerating outflows (Steidel et al. 2010).

This ejection of matter and energy into the IGM is also an important requirement for simulations of galaxy formation, where it is needed to regulate star formation. Feedback from supernovae in starbursts is required in semi-analytic models to reproduce the faint end of the present day galaxy luminosity function (e.g. Baugh et al. 2005). Hydrodynamical simulations have also shown that such winds can enrich the IGM with metals to levels required by observations (e.g. Theuns et al. 2002; Oppenheimer & Davé 2006).

LBGs close to background quasar sightlines allow us to measure the gas properties of the IGM close to galaxies, and search for any direct evidence of feedback and winds at $z \sim 3$. Adelberger et al. (2003) and Adelberger et al. (2005) (hereafter A03 and A05) pioneered the first of these analyses. By measuring the cross-correlation between H I Ly α absorption with nearby LBGs, they showed there is more Ly α absorption within $5 h^{-1}$ Mpc of LBGs compared to the mean absorption level. This was interpreted as clustering of H I gas around the galaxies, consistent with LBGs being found in overdense regions. For a significant fraction of LBGs within $1 h^{-1}$ Mpc of a quasar sightline, however, the observed absorption *decreased* substantially. This was interpreted as the background quasar sightline intercepting a bubble of ionized gas around some LBGs, possibly due to star formation feedback from these galaxies heating their surrounding IGM.

Winds were not expected to have such a large effect on the neutral hydrogen surrounding LBGs. Using a smoothed particle hydrodynamical (SPH) simulation Theuns et al. (2002) found winds had little effect on nearby H I absorption because they tended to deposit their energy into low density regions around the galaxy, leaving much of the H I gas undisturbed in filamentary structures. Subsequent theoretical SPH models (e.g. Bruscoli et al. 2003; Kollmeier et al. 2003; Kollmeier et al. 2006; Kawata & Rauch 2007) were also unable to reproduce the distribution of H I absorption close to LBGs measured by A03 and A05 without invoking exotic scenarios. Semi-analytic models (e.g. Desjacques et al. 2004; Bertone & White 2006) were able to reproduce the distribution, but these assumed spherical symmetry, and so side-stepped the geometrical considerations above.

Uncertainties in the galaxy redshift or Ly α absorption redshift can have a large influence on their cross-correlation at small scales. Such uncertainties are caused by redshift measurement errors and any intrinsic velocity dispersion between the galaxies and nearby absorbing H I gas. If there is a narrow feature in the real-space cross-correlation, it will be suppressed by velocity dispersions when it is measured in redshift-space. It is important to include these effects when attempting to reconstruct the real-space correlation function from that measured in redshift-space.

We have undertaken a program to observe LBGs with the Visible Imaging & Multi-Object Spectrograph (VIMOS) on the Very Large Telescope (VLT). This program will assemble a spectroscopic sample of $z \sim 3$ LBGs over nine fields, each chosen to be centred on a bright ($R \sim 18$) background quasar with emission redshift $\gtrsim 3$, most of which have archived echelle spectra available. The total area covered by the nine fields is $\sim 3.17 \text{ deg}^2$, corresponding to 45 VIMOS pointings. In addition to the central bright background quasar, we have assembled a further spectroscopic sample of $R \sim 19\text{--}20$, $z \sim 3$ quasars in each field. With these data we intend to measure the galaxy-galaxy and galaxy-IGM clustering properties at redshifts $\sim 2.5\text{--}3$. We shall both extend the A03, A05 data samples to larger LBG-LBG and Ly α -LBG transverse separations, and increase the number of known small separation LBG-quasar sightline pairs at $z \sim 3$.

In this paper we present spectroscopy of the quasars inside and around our LBG fields, describe the selection of quasar candidates and list the new quasars we have identified. Our analysis focuses on the small scale correlations between LBGs and the Ly α forest at separations $< 10 h^{-1}$ Mpc. We compare our results to simple models and the results of A03 and A05. The paper is structured as follows: in Sections 2 and 3 we describe the galaxy and quasar samples used in our analysis. In Section 4 we describe the quasar spectra. Sections 5 and 6 present measurements of the C IV-LBG cross-correlation and Ly α auto-correlation. Section 7 presents the main result of our paper, the cross-correlation between Ly α transmissivity and LBGs. Section 8 summarises the main findings of the paper.

We assume a cosmology with $\Omega_m = 0.3$, $\Omega_\Lambda = 0.7$ and $H_0 \equiv 100 h \text{ km s}^{-1} \text{ Mpc}^{-1}$, where Ω_m and Ω_Λ are the ratios of the matter density and cosmological constant energy density to the critical density. Unless stated otherwise all distances are comoving, and magnitudes use the AB sys-

tem, or asinh system for Sloan Digital Sky Survey (SDSS) magnitudes.

2 GALAXY SAMPLE

We obtained galaxy spectra for this project using the VIMOS multi-object spectrograph on the VLT. A detailed description of the LBG selection and sample properties is given by Bielby et al. (2010). In short, galaxies were selected using the Lyman break technique (e.g. Steidel et al. 1996), yielding a sample with $2.2 < z < 3.5$. Deep *UBR* or *UBVI* imaging was used to select LBG candidates, and these candidates were observed with the VIMOS multi-object spectrograph at a resolution of 180. In this paper we use the initial set of LBG data presented by Bielby et al. It contains 1020 LBGs with spectroscopic redshifts $z > 2$ spread across 19 VIMOS pointings in a total area of 1.44 deg^2 , over five of the nine fields that make up the complete survey area.

For our present analysis we are most concerned with uncertainties on the measured LBG redshifts. There are several contributions to the redshift uncertainty; Bielby et al. quote $\sim 150 \text{ km s}^{-1}$ due to the wavelength calibration, $\sim 450 \text{ km s}^{-1}$ from centroiding the Ly α emission lines, and $\sim 200 \text{ km s}^{-1}$ uncertainty in transforming from the emission and absorption redshifts to the intrinsic galaxy redshift. They estimate a total error of $\sim 500 \text{ km s}^{-1}$ in their measured intrinsic LBG redshifts, corresponding to $\Delta z = 0.007$ at $z = 3$.

3 QUASAR SAMPLE

Our quasar sample consists of $R < 22$ quasars with emission redshifts $2 < z < 4$ in and around five LBG fields where we have reduced galaxy spectra, and in four further fields that have as yet unreduced LBG observations. These consist of:

(1) Bright quasars at the centre of each LBG field. The LBG fields were chosen to be centred around bright quasars with emission redshifts $3 < z_{\text{em}} < 4$ and over a wide RA range to enable observations to be made throughout the year. The central quasars in the five LBG fields analysed in this paper are Q0042–2627, J0124+0044, HE0940–1050, PKS2126–158 and J1201+0116. Archived echelle spectra taken using the Ultraviolet Echelle Spectrograph (UVES) on the VLT or the HIRES spectrograph on the Keck Telescope exist for most of these quasars. The echelle spectra have resolution $> 30,000$ and hence resolve the linewidths of H I lines in the Ly α forest. There are four further fields where we will soon obtain LBG redshifts; around the central bright quasars Q0301–0035, Q2231–0015, Q2348–011 and Q2359+0653. Details for all nine central bright quasars are given in Table 1.

(2) Previously-known quasars in and around each field. In addition to the central bright quasars, we searched for any other known quasars with the appropriate redshift and magnitude in either the NASA Extragalactic Database¹ or

the survey by Worseck et al. (2008).

(3) New quasars discovered in each field. We obtained spectra for further quasar candidates in and around the LBG fields, selected from a variety of imaging sources.

We conducted a spectroscopic quasar survey targeting previously-known quasars and quasar candidates using the AAOmega spectrograph on the Anglo-Australian Telescope. AAOmega is a fibre-fed, multi-object spectrograph (Saunders et al. 2004; Smith et al. 2004; Sharp et al. 2006) with a resolution of 1300 for the 385R and 580V gratings we used during most of our observations. In a single pointing, up to 400 fibres can be targeted on objects over a circular field of view with radius of one degree.

3.1 Quasar selection for our AAOmega survey

To cross-correlate LBG positions with quasar absorption, we need background quasars with an emission redshift such that the Ly α forest overlaps the redshift range of our LBG sample and a bright enough magnitude to obtain the signal to noise ratio (S/N) required to measure Ly α forest absorption. An emission range of $2.5 < z_{\text{em}} < 4$ satisfies the first constraint – at lower redshift only a small portion of the forest remains above the atmospheric cutoff; at higher redshift the higher order Lyman transitions and Lyman limit absorption from redshifts > 4 make it difficult to identify Ly α absorption at the LBG redshifts. We chose a magnitude limit for candidates of $R = 22$; this was motivated by the S/N achievable over the Ly α forest in several hours of exposure using AAOmega. Wolf et al. (2003) estimate a sky density for quasars with $z > 2.2$ and $R_{\text{Vega}} < 22$ of $\sim 40 \text{ deg}^{-2}$, thus we anticipated there would be up to ~ 10 such quasars inside one of our typically $0.5 \times 0.5 \text{ deg}^2$ LBG fields.

To select candidates we used the theoretical quasar tracks in *ugr* colour space from Fan (1999, see his fig. 13) as a guide. Our criteria for candidates were that they were (1) point-like, (2) outliers in *ugr* colour space from the stellar locus, with the expected colours for $2.5 < z < 4.0$ quasars, and (3) had $r < 22$. The first two criteria are known to select quasars with redshifts > 3.0 with a relatively high completeness and efficiency for targets with $i < 20.8$ selected using SDSS imaging [Richards et al. (2002), but see also Worseck & Prochaska (2010)]. For $2.5 < z < 3.0$, the expected position of quasars in *ugr* colour space overlaps with A, F and horizontal giant branch stars, making efficient selection difficult. In an attempt to find a significant number of the available quasars in this redshift range, we included objects as close to the stellar locus as was possible without introducing an unacceptably large level of contamination. However, the efficiency of our quasar selection in this range is poor.

When possible, we checked that any known quasars in our fields were recovered by our selection process. This sometimes led us to adjust our colour cuts to ensure that known quasars in the desired redshift range were included using our selection criteria. We also adjusted colour cuts to provide a sufficiently high sky density of targets (~ 600 over the AAOmega field of view) that allowed CONFIGURE², the

¹ <http://nedwww.ipac.caltech.edu/>

² http://www.aao.gov.au/AAO/2df/aaomega/aaomega_manuals.html

Name	R.A. (J2000)	Dec (J2000)	z	Mag.	Instrument	Archived spectra PI	ID
Q2359+0653	00:01:40.6	+07:09:54	3.23	$V = 18.5$	-	-	-
Q0042-2627	00:44:33.95	-26:11:19.9	3.289	$B_j = 18.47$	HIRES	Chaffee	K01H
J0124+0044	01:24:03.78	+00:44:32.7	3.83	$g = 19.2$	UVES	Bouché	073.A-0653
Q0301-0035	03:03:41.05	-00:23:21.0	3.23	$g = 17.6$	HIRES	Prochaska	U11H
HE0940-1050	09:42:53.50	-11:04:25.9	3.06	$B = 17.2$	UVES	Bergeron	166.A-0106
J1201+0116	12:01:44.37	+01:16:11.7	3.233	$g = 17.7$	HIRES	Prochaska	U012Hb
PKS2126-158	21:29:12.15	-15:38:40.9	3.268	$V = 17.3$	UVES	Bergeron	166.A-0106
Q2231-0015	22:34:08.99	+00:00:01.7	3.02	$r = 17.29$	UVES	D'Odorico	65.O-0296
Q2348-011	23:50:57.9	-00:52:10	3.0235	$r = 18.68$	UVES	Ubachs	079.A-0404

Table 1. The nine central bright quasars around which LBG fields were targeted. The fourth and fifth columns give the emission redshift and a rough estimate of the quasar magnitude. The last three columns give the instrument, principle investigator and unique ID number for the archived observations where they are available.

software used to assign objects to the AAOmega fibres, to maximise the number of fibres used. Due to restrictions on fibre placement not all possible candidates could be observed. In general we prioritised brighter quasar candidates with $r < 21.5$, those with photometric redshift estimates, and those close to areas where LBG redshifts were to be measured.

Finally, for repeat observations of the same field we performed an initial identification of objects in the first set of observations. Any targets that could not be identified as quasars in the required redshift range were removed and replaced with new candidates for subsequent observations. If this exhausted our candidate list in a field, we adjusted the colour cuts closer to the stellar locus to provide more candidates.

Selection of quasars overlapping the LBG fields

To select quasars overlapping the LBG fields we generally used the same *UBR* or *UBVI* imaging that was used to select the LBG candidates (see Table 2). Selections in the central fields around Q0042-2627, Q0301-0035, J0124+0044, J1201+0116, PKS2126-158, Q2359+0653 were performed using the imaging data from the MOSAIC imagers at Kitt Peak National Observatory (KPNO) and the Cerro-Tololo Inter-American Observatory (CTIO) described by Bielby et al. (2010). This imaging covers a $32' \times 32'$ region around the central quasar. We used archived imaging taken with the Wide Field Camera on the Isaac Newton Telescope (INT) for the Q2231-0015 field. SExtractor (Bertin & Arnouts 1996) catalogues were generated from the images. For the HE0940-1050 and Q2348-011 fields, the central field selection was performed using archived *ugr* imaging data from the MegaCAM instrument at the Canada-France-Hawaii Telescope (CFHT) rather than the MOSAIC imaging used to select LBGs. The MegaCAM data reaches a similar depth to the MOSAIC data, but extends over a larger field of view, $1^\circ \times 1^\circ$.

The colour cuts we used to select quasar candidates varied slightly between fields, depending on the quality of the imaging, how well the photometric zero points had been measured, and the filters used. As an example, the cuts for the MegaCAM images in the HE0940-1050 field were:

- $18 < r < 22$

- $g - r < 1.1$
- $g - r < 0.54(u - g) - 0.35$, or $g - r < 0.15$
- $u - g > 0.6$

They are shown in the left panel of Fig. 1 as dashed lines, along with similar cuts for the other field with central MegaCam imaging, Q2348-011. Candidates were required to be detected in g and r , but we included candidates undetected in u if they satisfied the above criteria. The precise selections used for the MOSAIC data are given by Bielby et al. (2008, PhD thesis).

In total we obtained spectra of 50 $z > 2.2$ quasars overlapping the LBG fields in addition to the nine central bright quasars. Closed triangles in Fig. 1 show such quasars in the cases of the HE0940-1050 and Q2348-011 fields. Across all nine fields, 30 of these 50 were previously unknown quasars uncovered using the selection process above; the remainder were previously known. The total LBG area is 3.17 deg^2 , over which we obtained a quasar sky density of $\sim 18.6 \text{ deg}^{-2}$.

In the five fields we use for the cross-correlation analysis there are 16 $z > 2.2$ quasars. All of these were previously known. The Q0042-2627 field has been searched for quasars by Williger et al. (1996), and the HE0940-1050 and PKS2126-158 fields by Worseck et al. (2008), leaving few new quasars to be found. However, our sky densities in these fields are also low compared to other fields in the LBG area; the five fields cover 1.44 deg^2 giving a density of 11.1 deg^{-2} , much lower than the 18.6 deg^{-2} above. This lower density is in part due to the absence of any new quasars in the J0124+0044 central area beyond the central bright quasar. We are unsure of the reason for this. However, similarly large areas with very few quasars are present in the Q0301-0035 and Q2348-011 fields, which have deep Stripe 82 imaging across the entire AAOmega field. Clustering may be responsible for the clumpy quasar distribution, and it may simply have been unfortunate that a region largely empty of quasars occurs in the J0124+0044 LBG area.

Selection of quasars around the LBG fields

There were not enough quasar candidates overlapping each LBG area to employ all the AAOmega fibres, so we searched for candidates outside each LBG field over the full 3.1 deg^2 AAOmega field of view. Our motivation for finding quasars with angular separations of tens of arcminutes from LBGs

Field	Source	Central Imaging			Surrounding Imaging		
		Bands	Area	Depth	Source	Bands	Depth
Q2359+0653	MOSAIC	<i>UBR</i>	$32' \times 32'$	$R = 25$	Schmidt	<i>BR</i>	$R = 21$
Q0042-2627	MOSAIC	<i>UBR</i>	$32' \times 32'$	$R = 24.7$	Schmidt	<i>BR</i>	$R = 21$
J0124+0044	MOSAIC ^a	<i>UBVI</i>	$32' \times 32'$	$I = 24.5$	SDSS Stripe 82	<i>ugriz</i>	$r = 24.7$
Q0301-0035	MOSAIC	<i>UBR</i>	$32' \times 32'$	$R = 25$	SDSS Stripe 82	<i>ugriz</i>	$r = 24.7$
HE0940-1050	MegaCAM	<i>ugri</i>	$1^\circ \times 1^\circ$	$r = 24.7$	Schmidt	<i>UBR</i>	$R = 21$
J1201+0116	MOSAIC	<i>UBR</i>	$32' \times 32'$	$R = 25.5$	SDSS	<i>ugriz</i>	$r = 22.6$
PKS2126-158	MOSAIC	<i>UBR</i>	$32' \times 32'$	$R = 24.7$	Schmidt	<i>UBR</i>	$R = 21$
Q2231-0015	WFC	<i>UBR</i>	$32' \times 32'$	$r = 25$	SDSS	<i>ugriz</i>	$r = 22.6$
Q2348-011	MegaCAM	<i>ugri</i>	$1^\circ \times 1^\circ$	$r = 25$	SDSS Stripe 82	<i>ugriz</i>	$r = 24.7$

Table 2. Imaging used to select quasar candidates inside the central LBG regions and surrounding the central regions. The different bands available, the area of the central imaging and depths are also shown. Depths give approximate 50% completeness depth (MOSAIC, SDSS, Stripe 82, MegaCAM, INT) or the magnitude limit (Schmidt). The image source abbreviations are; MOSAIC: the imaging was taken with the MOSAIC imager at either CTIO or KPNO; Schmidt: catalogues generated from Schmidt plates were used; MegaCAM: archived CFHT MegaCAM imaging; WFC: archived INT Wide Field Camera observations; SDSS: single epoch SDSS imaging; SDSS stripe 82: multi-epoch SDSS imaging in Stripe 82. ^a For the J0124+004 field, we selected targets in the central region from an object catalogue generated from MOSIAC imaging; see Bielby et al. (2010) and Bouché & Lowenthal (2004) for details.

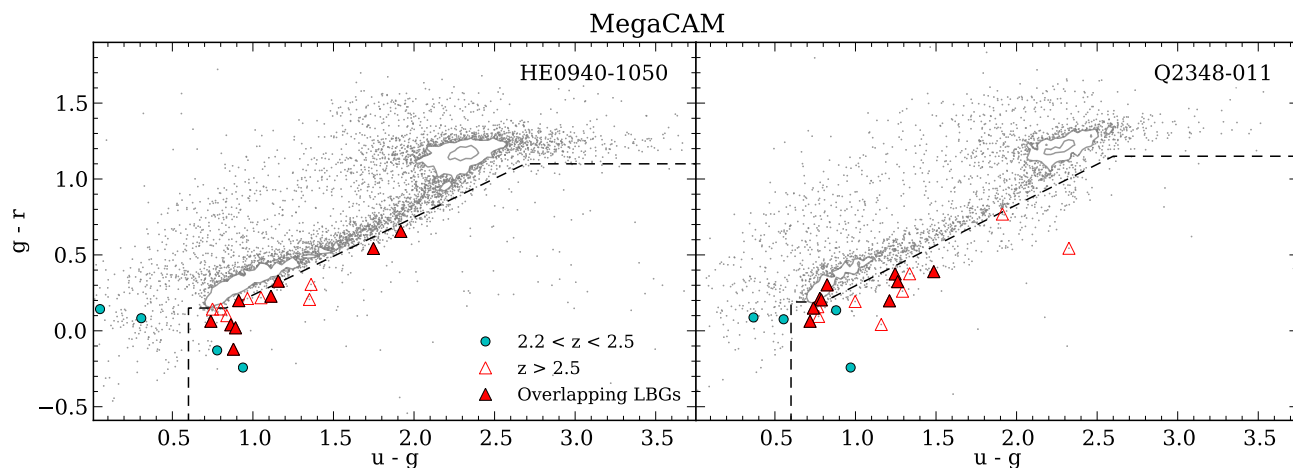


Figure 1. Colour cuts used for $1^\circ \times 1^\circ$ CFHT MegaCam data in the HE0940-1050 and Q2348-011 fields. Grey points and contours show all stellar objects (SExtractor CLASS_STAR > 0.85) with $r < 22$. Objects below the borders marked by the dashed line were selected as quasar candidates. Triangles show known quasars with $z \geq 2.5$, and circles show quasars with $2.2 \leq z < 2.5$. Open triangles are quasars outside the area where we have LBG observations; solid triangles are quasars overlapping the LBG fields on the sky.

was not to look for the effects of feedback – the IGM probed is much further from the LBGs than the distances across which winds are expected to have a significant effect. However, with a large number of $z \sim 3$ quasars over a few square degrees we can measure correlations in metal or forest absorption on scales of tens of Mpc due to large scale structure (Williger et al. 2000), constrain the 3-d topology of the IGM (Pichon et al. 2001) and measure large scale anisotropies in the 2-d LBG-Ly α correlation function caused by velocity dispersion and infall. These projects are beyond the scope of our current analysis, but our quasar sample provides a valuable resource for future studies.

The deep imaging used to select LBGs does not extend across the full AAOmega field of view, so we used different imaging sources to select candidates outside the central LBG regions. For the J0124+0044, Q0301-0035, J1201+0116, Q2231-0015 and Q2348-011 fields we used single epoch SDSS *ugr* imaging catalogues. Quasar can-

didates were selected in three ways. Firstly, we targeted any of the photometrically-selected quasar candidates from Richards et al. (2004) and Richards et al. (2009) with appropriate photometric redshifts. Secondly, we used the SDSS pipeline classifications (Richards et al. 2002): objects were classified in the SDSS reduction pipeline as quasar candidates based on their colours, stellar/non-stellar classification and radio detection. Only candidates with $i < 20.2$ were followed up for spectroscopy by the SDSS, leaving many fainter candidates without spectra. Any of these with colours consistent with our desired redshift range were added to our target list. Finally, we selected additional candidates not already selected by the above two methods using our own *ugr* colour cuts. Fig. 2 shows colour-colour plots for these five fields with single-epoch SDSS imaging. The points and contours show SDSS stellar objects and the *ugr* selection cuts we used are shown by dashed lines. Quasars we observed, both previously-known and newly discovered, inside

and outside the LBG areas, are shown as triangles and circles.

Three of our equatorial fields (J0124+0044, Q0301–0035 and Q2348–011) overlap the Stripe 82 region, where repeat SDSS observations were taken for the Supernova Survey (Frieman et al. 2008). In these fields we selected candidates using catalogues generated by combining the multi-epoch imaging. For J0124+0044 and Q2348–011 we offset the AAOmega pointing centre from the central bright quasar to maximise overlap with the Stripe 82 catalogue. The *ugr* cuts used to select candidates from the Stripe 82 catalogues are shown by dashed lines in Fig. 3. These cuts were modified slightly from those used on other imaging catalogues to include a box with $0.5 < u - g < 0.75$ and $0.2 < g - r < 0.4$, based on the colours of photometrically-selected targets from Richards et al. (2009).

Where SDSS imaging was not available (Q0042–2627, HE0940–1050, PKS2126–158 and Q2359+0653 fields), we used *B* and *R* catalogues generated from Schmidt photographic plates processed by the automated plate measuring machine. For the HE0940–1050 and PKS2126–158 fields we also had access to Schmidt *U* catalogues. Candidates were selected using similar criteria to the central areas where *U* imaging was available or using only *B* – *R* cuts otherwise.

In total we obtained spectra for 193 $z > 2.2$ quasars outside the LBG areas. 134 of these are newly discovered: 31 photo-*z* candidates from single epoch SDSS imaging, 21 selected from deep LBG imaging that extended beyond the LBG areas, 40 using *ugr* cuts with Stripe 82 imaging, 28 selected using similar cuts with single epoch SDSS imaging and the remaining 14 from Schmidt imaging.

3.2 Catalogue of quasars found in the AAOmega survey and completeness

Our AAOmega survey obtained spectra of 243 $z > 2.2$ quasars, of which 164 are newly discovered. The number of quasars found per field and their selection source are given in Table 3, and their details are in Table C1. Their magnitude and redshift distributions are shown in Fig. 4. Some quasars with $2.1 < z < 2.5$ were also recovered by our selection criteria for $z > 2.5$ quasars. Even though little of their Ly α forest is observable above the atmospheric cutoff, they are still useful for other purposes such as identifying C IV absorption near LBGs, or cross-correlating AGN with LBGs. There are also 10 faint $R \gtrsim 22$ quasars overlapping the LBG areas in Table C1 that we discovered in our VIMOS observations. We do not use these in the present analysis; they are described further by Bielby et al. (2010).

The right ascension and declination of quasars and LBGs in each field are shown in Fig. 5 to 7. It is apparent from these figures that our quasar sample is not uniformly distributed on the sky. This is mostly due to the variable imaging depths used in the different fields; few quasars were found outside the LBG regions in the J1201+0116 and Q2359+0653 fields, where only Schmidt imaging was available, but we achieved a much higher density in the J0124+0044, Q0301–0035 and Q2348–011 fields where Stripe 82 imaging was available across the entire field. However, as we remarked earlier, there are large regions free from quasars even in areas where we have deep imaging.

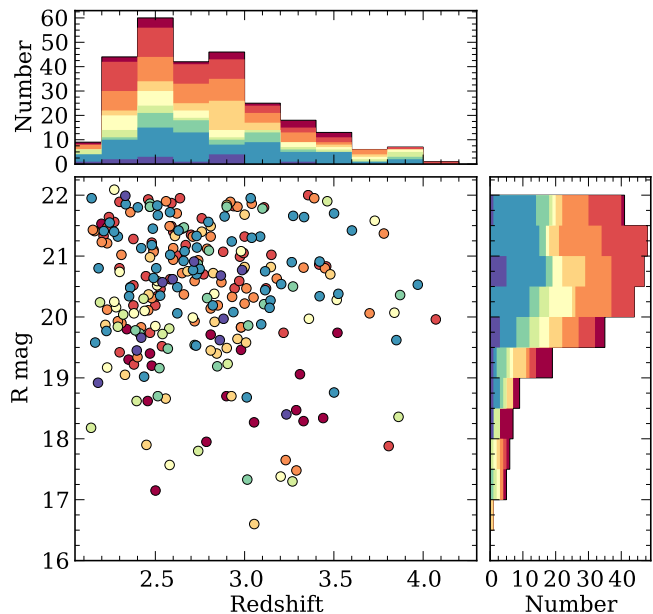


Figure 4. The redshift and *R* magnitude distribution for quasars with $R < 22$ and $z > 2.2$ in nine AAOmega fields. Each colour represents quasars from a different field. From the top of the histogram to the bottom, colours denote the Q0042–2627, J0124+0116, Q0301–0035, HE0940–1050, J1201+0116, PKS2126–158, Q2231–0015, Q2348–011 and Q2359+0653 fields.

This may be due in part to large scale structure and quasar clustering.

We can roughly estimate our sample’s completeness – the fraction of the total number of quasars in our redshift range and to our magnitude limits we have recovered – by comparing our sky densities to those for the COMBO-17 quasar survey (Wolf et al. 2003). Wolf et al. measured the number density of $R_{\text{Vega}} < 22$ quasars with $z > 2.2$ to be ~ 40 per square degree. In Fig. 8 we show the cumulative sky densities for quasars in the central region of each of our nine fields, where deep imaging was used to select quasar candidates, compared to the incompleteness-corrected sky densities found by Wolf et al. (see their table 3). Up to $R = 21$, our densities are consistent, suggesting our completeness is high. At $R = 22$, our sky densities drop to 50% of those found by Wolf et al., suggesting we recover only 50% of these fainter quasars. This low completeness level is not surprising: for single-epoch SDSS candidates we prioritised bright ($R < 21.5$) targets and did not observe many fainter targets; a significant fraction of candidates overlaps with the stellar locus; and for very faint targets even if a quasar was observed in poor conditions, we may have failed to identify it. For areas outside the central deep imaging, our completeness will be much poorer. Appendix A describes the efficiency of our quasar selection process and suggests ways to improve the selection efficiency for $2.5 < z < 4.0$ quasars in future surveys.

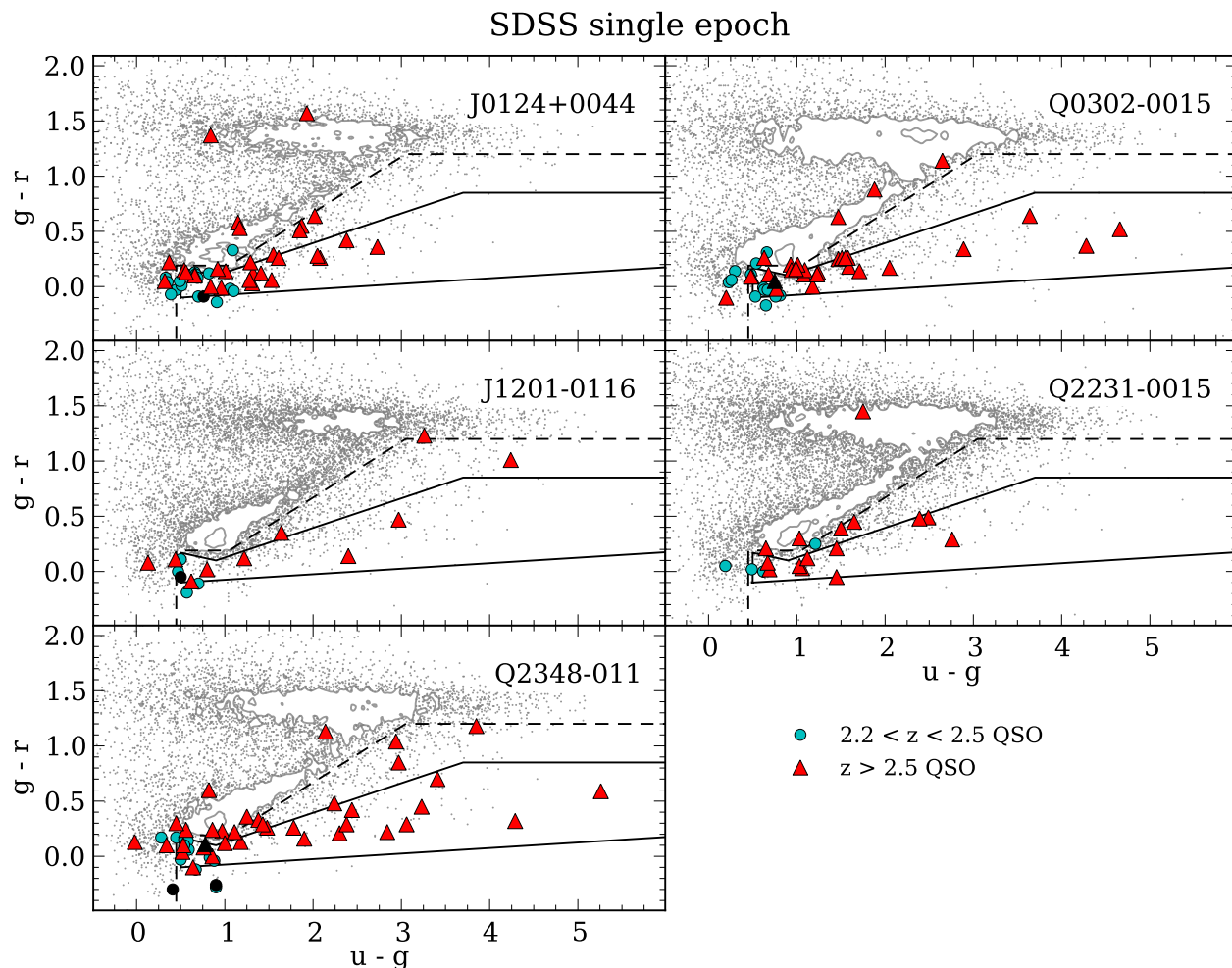


Figure 2. Colour cuts for used for single-epoch SDSS data in the J0124+0044, Q0301–0035, J1201+0116, Q2231–0015, and Q2348–011 fields. Objects classified by the SDSS pipeline as stellar with $r < 22$ are shown by the grey points and contours. Objects below the borders marked by the dashed line were selected as quasar candidates. The solid line shows the region used to select candidates for the efficiency calculations in Appendix A. Triangles show known quasars with $z > 2.5$, and circles known quasars with $2.2 < z < 2.5$. Several of these quasars were classified in SDSS single epoch imaging as non-stellar; they are shown by black circles and black triangles. They were included in our sample because of alternative selection criteria.

4 QUASAR SPECTRA

4.1 High resolution quasar spectra

UVES archived spectra are available for the bright central quasars J0124+0044, HE0940–1050 and PKS2126–158 and Keck/HIRES archive spectra are available for Q0042–2627 and J1201+0116. These spectra have resolution full widths at half maximum (FWHM) of $6 - 8 \text{ km s}^{-1}$. The UVES spectra were reduced using the UVES pipeline, and individual exposures were combined with UVES POPLER software³. The Keck spectra were reduced using the MAKEE package⁴. In addition we have obtained HIRES spectra for bright quasars in the Q0042–2627 and PKS2126–158 fields; [WHO91] 0043–265, with emission redshift $z = 3.45$,

and Q212904.90–160249.0, with $z = 2.94$. Archived high-resolution spectra are also available for the central bright quasars in the four fields without LBG data; these will be presented in a future paper.

The observations of [WHO91] 0043–265 and Q212904.90–160249.0 were taken on the night of the 22nd of August 2007 using Keck/HIRES with the red cross-disperser and C1 dekker, giving a slit width of 0.861 arcsec and resolution of 6.7 km s^{-1} . Exposures were extracted and wavelength calibrated using the MAKEE package.

Fig. 9 shows the final reduced echelle spectra. In some of the spectra there are breaks in the wavelength coverage. These are due to either separate wavelength settings that did not overlap, gaps between the CCD detectors, or regions where echelle orders were too wide to be completely recorded by the detector.

³ http://astronomy.swin.edu.au/~mmurphy/UVES_popler

⁴ <http://spider.ipac.caltech.edu/staff/tab/makee/>

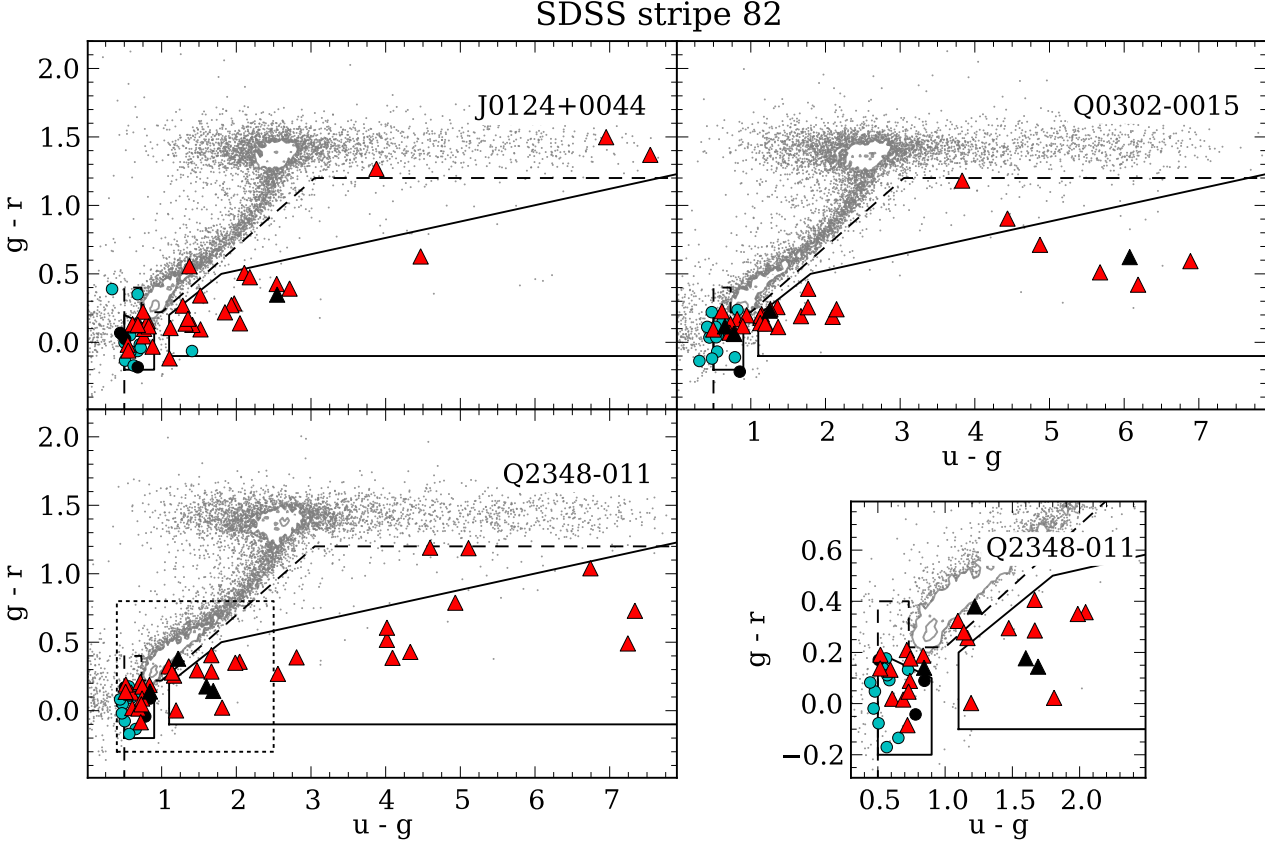


Figure 3. Colour cuts for used for multi-epoch Stripe 82 SDSS data in the J0124+0044, Q0301–0035, and Q2348–011 fields. The lines and symbols are the same as in Fig. 2. The bottom right panel is a zoomed plot of the dotted region shown in the bottom left panel.

4.2 Lower resolution quasar spectra

G. Williger kindly provided us with electronic versions of the spectra that overlap the Q0042–2627 LBG field (Williger et al. 1996). These spectra had been extracted, wavelength calibrated and flux calibrated. They have a typical S/N of ~ 20 per 1 \AA pixel, and resolution FWHM of $\sim 2 \text{ \AA}$. Quasars for which these spectra are available are marked by ‘Wil’ in the comment field of Table C1.

The remaining low resolution spectra were obtained with AAOmega. Each night of the AAOmega observations, arcs and flat fields were taken for every wavelength setting used. The central coordinates, exposure times per grating for each field and observation dates are shown in Table 4. For the initial observations we used the blue 1500V grating (resolution 3700) and red 1000R grating (resolution 3500) covering wavelengths 4230–6860 \AA . However, for faint quasars the S/N at wavelengths covering the Ly α forest, 4230–5700 \AA , was poorer than anticipated. Therefore for the majority of our observations we used the lower resolution blue (580V) and red (385R) gratings. Both have a resolution of 1300 and together provide a wavelength range of 3750–8900 \AA . In addition to enabling better S/N at wavelengths corresponding to the Ly α forest, the larger wavelength range for these gratings allowed us to identify more emission features, and thus make more secure quasar identifications.

4.3 Reduction of AAOmega spectra

AAOmega spectra were reduced using the 2DFDR program⁵. Each set of AAOmega observations consists of science, arc and flat field exposures for the blue and red gratings. 2DFDR processes each science image by subtracting a combined bias image, dividing by a combined flat field, tracing and rectifying the spectrum of each object and generating a wavelength solution using an arc exposure. Finally it extracts each spectrum, producing a 1-d spectrum for each fibre. The RMS for the wavelength solution for an AAOmega spectrum was typically 0.2 pixels, corresponding to $\sim 15 \text{ km s}^{-1}$. Once the 1-d spectra were extracted, we used 2DFDR to combine spectra taken on the same night using the same grating and wavelength setting into a single spectrum.

The final reduction steps removed the instrumental response from the spectra and combined the multiple wavelength settings. For our analysis we are interested in the absorption properties along each sightline, which do not require an accurate flux calibration. However, we still performed an approximate correction for the instrumental response to guide our object identification and continuum fitting. For most of the AAOmega pointings we targeted a bright quasar with an existing flux-calibrated spectrum in

⁵ http://www.aao.gov.au/AAO/2df/aaomega/aaomega_manuals.html

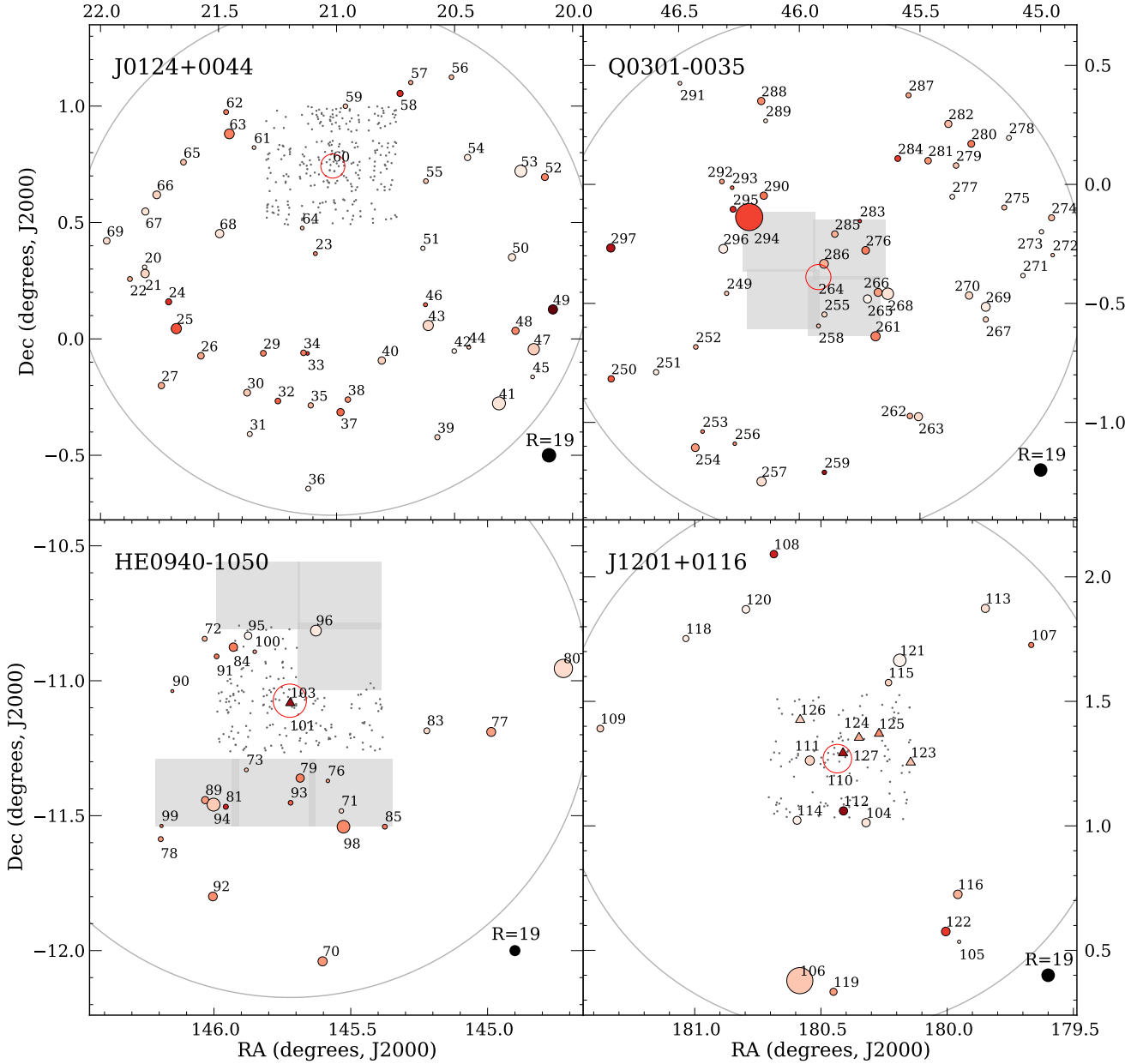


Figure 6. Quasar positions in the J0124+0044, Q0301-0035, HE0940-1050 and J1201+0116 fields. Grey shaded regions show observed VIMOS fields where spectroscopic LBG redshifts have not yet been measured. Other symbols are the same as in Fig. 5. The J0124+0044 pointing is offset from the central quasar to maximise overlap with Stripe 82 imaging.

the literature. We obtained an instrumental response curve for this quasar by dividing the AAOmega spectrum by the flux-calibrated spectrum, and applied this curve to the rest of the AAOmega spectra in that pointing. For pointings without a flux-calibrated target, we used a response curve from a similar observation taken during the same night.

For fields where we obtained spectra using both 1500V/1000R gratings and 580V/385R gratings, we only used spectra from the lower resolution gratings. The typical S/N per Å in our combined spectra was ~ 10 at $R = 19$, and ~ 3 at $R = 21$.

4.4 Measurement of quasar redshifts

We identified quasars in the required redshift range by their Ly α , C IV, Si IV and C III emission features and forest absorption. The identifications were performed by eye. We measured quasar emission redshifts by fitting a Gaussian profile to the C IV emission line where it could be measured, or C III when C IV was not usable. Care was taken to account for broad absorption that can shift the apparent position of emission peaks for broad absorption line (BAL) quasars; in these cases we fitted only the red wing of the emission line when measuring the emission line position.

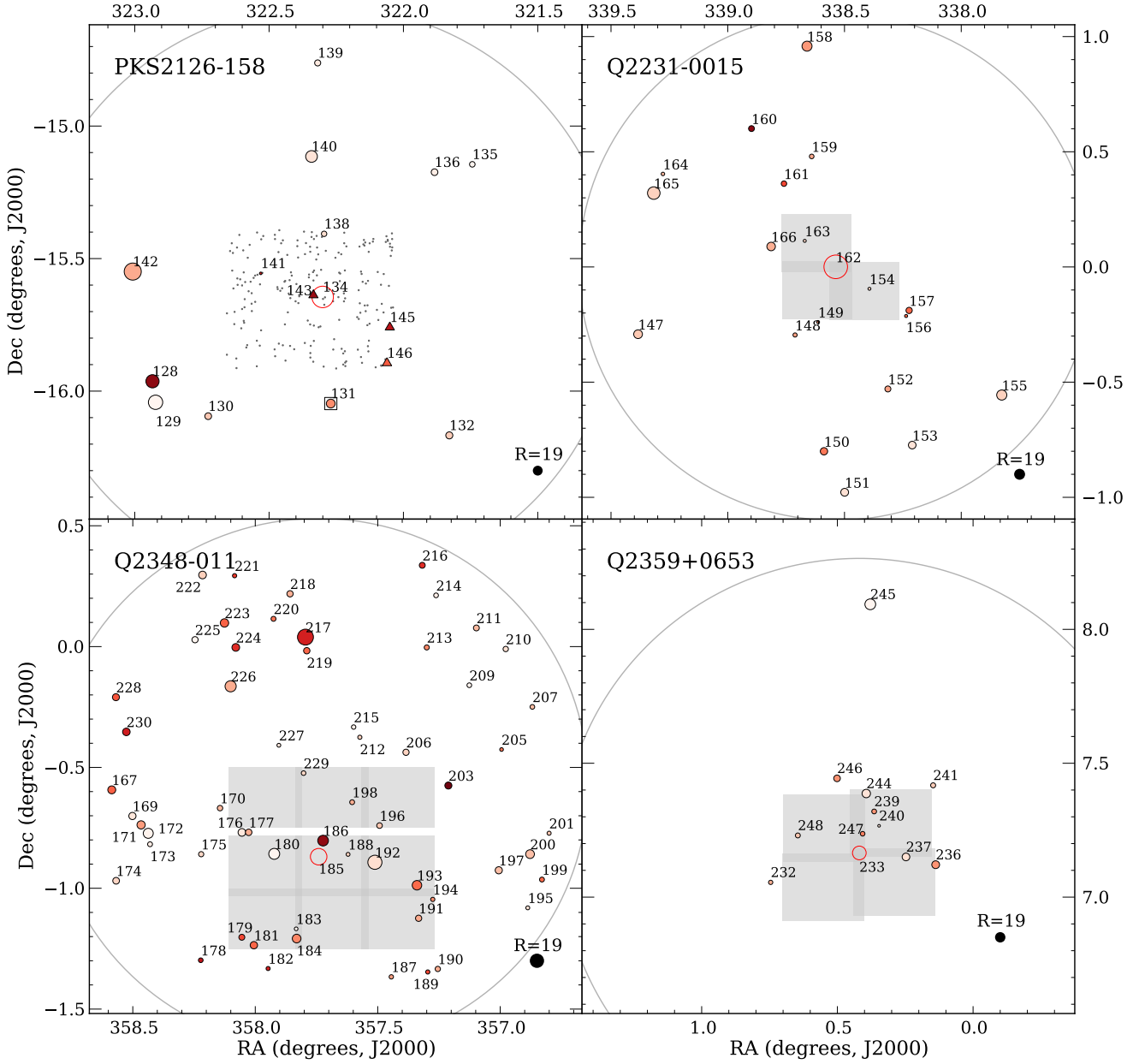


Figure 7. Quasar positions in the PKS2126–158, Q2231–0015, Q2348–011 and Q2359+0653 fields. The Q2348–011 pointing is offset from the central quasar to maximise overlap with Stripe 82 imaging. Symbols are the same as in Fig. 5 and 6.

4.5 Quasar continuum fitting

In order to perform the cross-correlation analysis, we require the transmissivity in the Ly α forest for each of the quasars. This is defined as

$$T = \frac{f}{f_c}, \quad (1)$$

where f is the measured flux and f_c is the flux level of the continuum (the intrinsic unabsorbed quasar spectrum) in the Ly α forest. We therefore require an estimate of f_c from the forest profile. To find this we perform a continuum fitting method based on that of Young et al. (1979) and Carswell et al. (1982).

First the quasar spectrum is split into wavelength intervals and the mean and standard deviation are calculated within each interval. Pixels that fall below the mean by more than an arbitrary factor n times the standard deviation are rejected, and the mean and standard deviation are re-calculated using the remaining pixels. This process is repeated iteratively until the remaining pixel fluxes show an approximately Gaussian distribution, with standard deviation equal to the expected 1σ flux errors. With the continuum level determined in these discrete intervals, a cubic spline was then used to interpolate across the whole of the spectrum. Finally, this continuum was adjusted by hand in regions where the fit still appeared poor, generally over

Field	R.A.	Dec.	Exposure time per grating (hours)					Dates observed
			580V c4800	385R c7300	1500V c4625	1500V c5365	1000R c6280	
Q2359+0653	00:01:45.87	+07:11:45.3	3.5	3.5	0	0	0	3 Jul 2008, 26 Oct 2008
Q0042-2627	00:44:34.00	-26:11:33.0	0	0	2.0	2.5	4.5	10-12 Jul 2007
J0124+0044	01:24:03.77	+00:20:32.7	6.0	6.0	0	0	0	24-25 Oct 2008
Q0301-0035	03:03:41.05	-00:23:21.8	6.0	6.0	0	0	0	24-26 Oct 2008
HE0940-1050	09:42:52.77	-11:04:19.9	1.5	3.5	5.0	0	3.0	18 Mar 2007, 5 Feb 2008
J1201+0116	12:01:43.90	+01:16:00.1	1.5	2.5	1.5	1.5	3.0	10-12 Jul 2007, 5-6 Feb 2008
PKS2126-158	21:29:12.40	-15:38:46.1	2.5	2.5	3.0	2.5	5.5	10-11 Jul 2007, 29 Jun 2008
Q2231-0015	22:34:09.16	+00:00:05.0	3.5	3.5	0	0	0	30 Jun 2008, 3 Jul 2008
Q2348-011	23:50:57.90	-00:34:10.0	6.5	6.5	0	0	0	2 Jul 2008, 24-26 Oct 2008

Table 4. Exposure times and central coordinates (J2000) for the AAOmega pointings. Note the central pointings do not always coincide with the positions of the bright central quasars in Table 1. The total exposure times for each combination of grating and central wavelength are shown. The final column gives the dates when each field was observed.

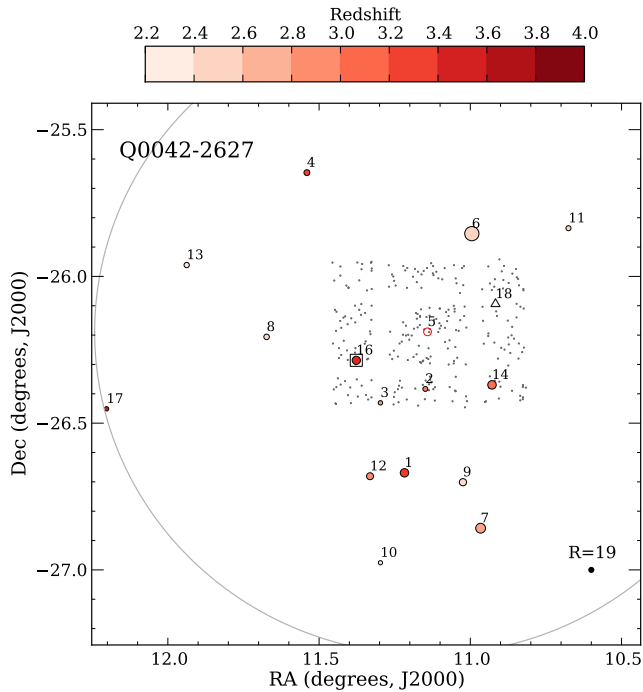


Figure 5. Quasar positions in the Q0042-2627 field. Grey dots show LBGs with spectroscopically-confirmed redshifts. Each quasar is labelled with its number from Table C1 and the open circle is the bright central quasar. Quasars surrounded by a square box (and the central quasar) have been observed at high resolution. The area of each circle is proportional to the R band quasar luminosity. The size of a quasar with $R = 19$ is shown at the bottom right for comparison. Triangles show very faint quasars ($R > 23$) that were discovered serendipitously in our VIMOS observations. North is up and East is to the left. The remaining eight fields are shown in Fig. 6 and 7.

damped $\text{Ly}\alpha$ absorption systems and emission lines. n was determined by trial and error; a typical value was 1.2, but the best value varied with the signal to noise ratio and resolution of the spectrum, and inside and outside the $\text{Ly}\alpha$ forest. The widths of the wavelength intervals were similarly chosen by trial and error. Narrow intervals were required

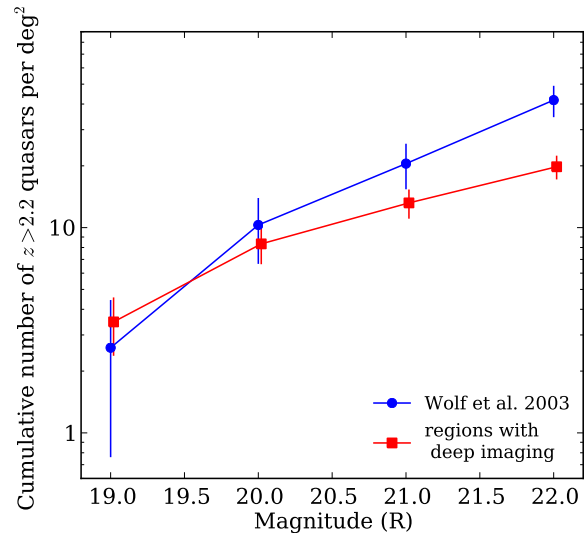


Figure 8. The cumulative sky densities of quasars with $z > 2.2$ as a function of magnitude from Wolf et al. (2003) compared to our quasar sample in regions where deep imaging (to $R \sim 25$) was used to select quasars. Our completeness is high up to $R \sim 21$, but drops to 50% at $R = 22$.

over emission features and wider intervals were appropriate for the $\text{Ly}\alpha$ forest.

The results of this fitting process for each of the central bright quasars and two non-central bright quasars observed at high resolution are shown in Fig. 9. Typical continua fitted to the fainter AAOmega survey quasars are shown in Fig. 10.

4.6 Damped $\text{Ly}\alpha$ and Lyman limit systems in the sample

During our analysis of spectra in the first five LBG fields we identified several candidate damped $\text{Ly}\alpha$ systems (DLAs) and sub-damped $\text{Ly}\alpha$ systems [also known as super Lyman limit systems (SLLS)]. Regions of the $\text{Ly}\alpha$ forest affected by strong DLA damping wings were removed for the correlation

Field	Type	Cand.	New	Known
Q0042–2627	Central			
	32' × 32'	12	0	
	<i>ugr</i>	263	0	
	Total	275	0	16
J0124+0044	Central			
	32' × 32'	19	0	
	Photo- <i>z</i>	92	14	
	Stripe 82	145	20	
	SDSS <i>ugr</i>	377	2	
	Total	633	36	13
Q0301–0035	Central			
	32' × 32'	129	5	
	Photo- <i>z</i>	80	8	
	Stripe 82	48	9	
	SDSS <i>ugr</i>	351	8	
	Total	608	30	16
HE0940–1050	Central			
	1° × 1°	113	14	
	Schmidt <i>UBR</i>	382	8	
	Total	479	22	2
J1201+0116	Central			
	32' × 32'	0	0	
	Photo- <i>z</i>	2	1	
	SDSS <i>ugr</i>	322	4	
	Total	324	5	13
PKS2126–158	Central			
	32' × 32'	346	2	
	Schmidt <i>UBR</i>	355	6	
	Total	701	8	3
Q2231–0015	Central			
	32' × 32'	77	4	
	Photo- <i>z</i>	2	0	
	SDSS <i>ugr</i>	83	5	
	Total	162	9	11
Q2348–011	Central			
	1° × 1°	219	16	
	Photo- <i>z</i>	49	8	
	Stripe 82	68	11	
	SDSS <i>ugr</i>	633	9	
	Total	969	44	13
Q2359+0653	Central			
	32' × 32'	251	10	
	Schmidt <i>BR</i>	360	0	
	Total	611	10	1
All		4762	164	88

Table 3. Quasar candidates observed with AAOmega, and the number of new quasars found. Columns show the field names, the candidate source, the observed candidates for that source, and the number of identified quasars with $z > 2.2$. The total number of observed candidates, new quasars and the number of quasars previously known in each field is also shown.

analysis. Such systems are of interest for potential follow-up studies with higher resolution spectroscopy and we list them in Table C2. Candidate systems were identified as strong Ly α absorption features with two or more associated metal features. We caution that the systems were identified by eye in spectra of varying quality and S/N, and thus are subject to selection biases.

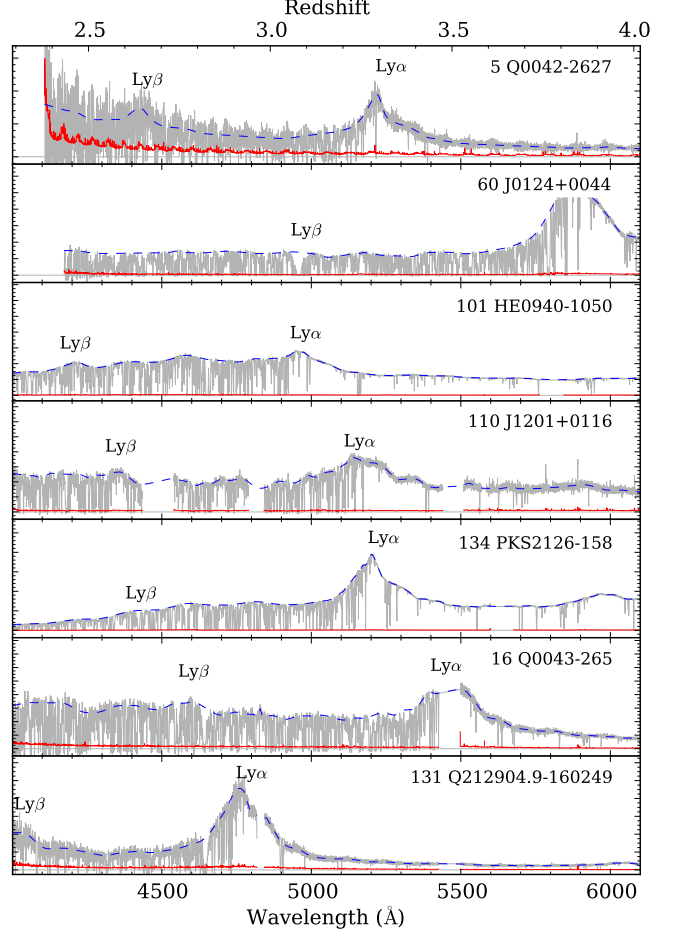


Figure 9. High resolution spectra of quasars overlapping or near our LBG fields. The top five panels show archived spectra of the central bright quasars in our five fields with reduced LBG data. The lower two panels show spectra of two non-central quasars we observed at high resolution: [WHO91] 0043–265, in the Q0042–2627 field, and Q212904.90–160249.0, in the PKS2126–158 field. The quasar Ly α and Ly β emission are labelled, and the number of each quasar from Table C1 is listed before the quasar name. Continua (dashed blue curves) and the 1σ error per $\sim 0.05\text{\AA}$ pixel are also shown.

4.7 Quasar sub-sample used in the LBG-Ly α cross-correlation

We constructed a sub-sample of quasars with a Ly α forest suitable for cross correlation with LBGs in the following way. We began with all quasars within $20'$ of a spectroscopically-confirmed LBG. From these we removed any quasars that were clearly broad absorption line quasars, showing very strong absorption in the blue wing of their C IV emission line.

In the remaining quasars we defined the Ly α forest region used to cross-correlate with the LBGs. We used only the quasar spectral range between the quasar Ly β and Ly α emission lines. By discarding the region below Ly β emission, we avoid any contamination of the Ly α lines by Lyman series lines from higher redshift forest absorbers. We also excluded the range within 3000 km s^{-1} of the quasar's Ly α emission

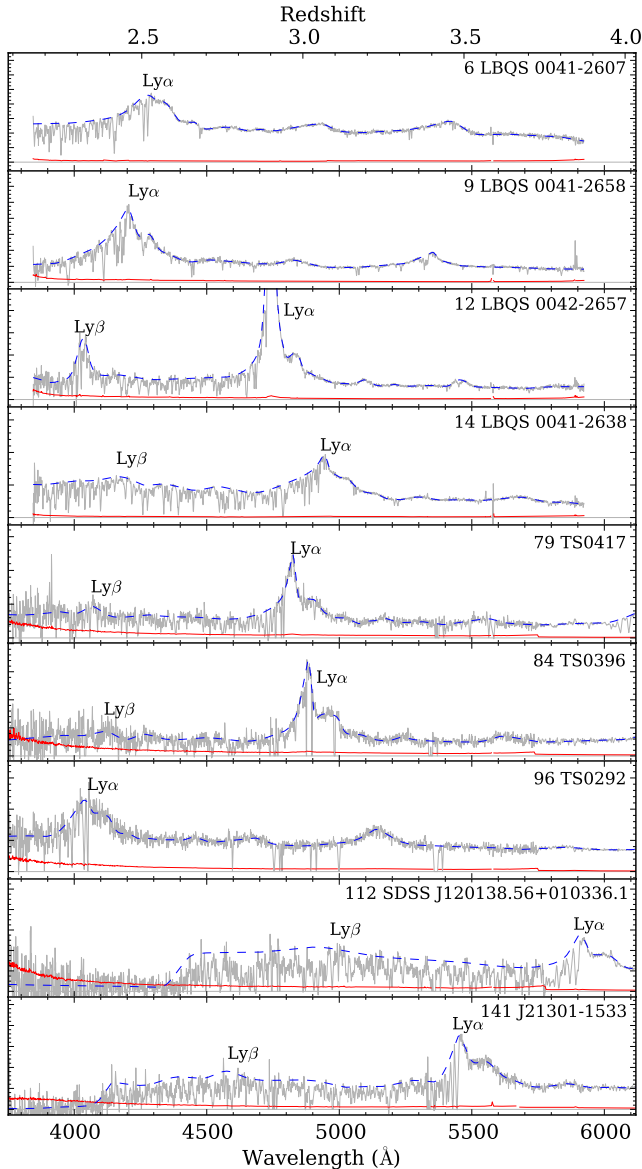


Figure 10. Low resolution spectra of quasars we used to measure the Ly α transmissivity as a function of distance from LBG. Only quasars that contribute to the Ly α -LBG cross-correlation on scales $< 20 h^{-1}$ Mpc are shown. The top four panels are spectra from Williger et al. (2000) in the Q0042–2627 field. The next three panels show our AAOmega spectra for three quasars in the HE0940–1050 field. The final two spectra are for quasars in the J1201+0116 and PKS2126–158 fields. The quasar Ly α and Ly β emission are labelled, and the number of each quasar from Table C1 is listed before the quasar name. Continua (dashed blue curves) and the 1σ error per ~ 1 Å pixel are also shown.

both to avoid absorbers affected by the ionising radiation from the background quasar, and to minimise the number of absorbers in our sample that may be ejected from the background quasar. Additionally, we removed any damped Ly α systems present in the spectra from the analysis.

We excluded any regions in either the low-resolution spectra where the S/N at the continuum is very poor (< 3 per pixel), or there were clearly problems with the reduction,

such as poor subtraction of sky lines. For such very low S/N regions the reliability of the continuum fit is likely to be low, and systematics associated with the data reduction process to be significant. For some quasars the entire Ly α region was removed due to poor S/N.

Any remaining quasars after applying the criteria above formed the sample we used to cross-correlate with LBG positions. This final sample was split into two further sub-samples; seven quasars with high resolution ($< 10 \text{ km s}^{-1}$) spectra and nine with low resolution ($> 100 \text{ km s}^{-1}$) spectra. As the systematic errors affecting the low resolution and high resolution samples are different, we calculate the cross-correlation for each sample separately. The quasars in each sample are given in Tables 5 and 6 and their spectra are shown in Fig. 9 and 10. For five quasars in the low resolution sample we use spectra taken in our AAOmega survey and for the remaining four we use spectra from Williger et al. (1996).

5 C IV – LBG CROSS-CORRELATION

Supernovae-driven winds are one of the processes believed to be able to enrich the IGM with metals. If they are a dominant mechanism for enriching the IGM, we might expect to see metal-rich gas surrounding LBGs, which are known to be undergoing significant star formation. The cross-correlation between C IV absorption systems and LBGs allows us to examine the clustering of metal enriched gas around known star-forming galaxies.

By analysing the projected transverse correlation function A03 found that on scales $< 5 h^{-1}$ Mpc, the clustering strength between LBGs and C IV systems was comparable to the LBG-LBG clustering strength for $\log N_{\text{C IV}} \sim 13$, smaller for smaller $\log N_{\text{C IV}}$ and larger for larger $\log N_{\text{C IV}}$. One explanation for this is that many of the strongest C IV systems arise in gas directly associated with LBGs seen in the same data sample, perhaps a larger scale extension of the winds inferred from C IV absorption in the LBG spectra. The weaker correlation at low $N_{\text{C IV}}$ may be explained by C IV arising in the same large scale structures as LBGs. By measuring absorption from foreground LBGs in the spectrum of a nearby ($< 10''$) background LBGs, A05 found that C IV gas with $\log N_{\text{C IV}} > 12.5$ is found around LBGs out to radius of 80 kpc. This analysis was recently extended to a larger sample of higher resolution LBG spectra by Steidel et al. (2010). We defer a similar analysis of our LBG spectra to a future paper. In this section we look for C IV absorption that may be associated with LBGs that are very close to background quasar sightlines, and measure the C IV-LBG cross-correlation for our sample.

5.1 Creating a C IV absorption line catalogue

We identified absorption due to the C IV $\lambda 1548, 1550$ doublet in background quasar spectra in the following way. First we identified significant absorption features in the quasar spectrum, then we scanned each spectrum to identify possible features that were part of a C IV doublet. For the lower resolution AAOmega spectra we also fitted Gaussian profiles to the absorption doublets. Finally we measured the rest

Num.	Name	Field	R.A. (J2000)	Dec (J2000)	z	Resolution (km s ⁻¹)	S/N (per pixel)
5	Q0042–2627	Q0042–2627	00:44:33.95	–26:11:19.9	3.29	6.7	8
16	[WHO91] 0043–265	Q0042–2627	00:45:30.47	–26:17:09.2	3.44	6.7	18
60	J0124+0044	J0124+0044	01:24:03.78	+00:44:32.7	3.81	7.5	38
101	HE0940–1050	HE0940–1050	09:42:53.50	–11:04:25.9	3.05	7.5	90
110	J1201+0116	J1201+0116	12:01:44.37	+01:16:11.7	3.20	6.7	24
131	Q212904.90–160249.0	PKS2126–158	21:29:04.90	–16:02:49.0	2.90	6.7	9
134	PKS2126–158	PKS2126–158	21:29:12.15	–15:38:40.9	3.27	7.5	100

Table 5. Quasars with high resolution spectra used to measure the cross-correlation between LBGs and the Ly α forest. These comprise the high resolution sample used for the correlation function in Fig. 13. Their spectra are shown in Fig. 9. Five of these (Q0042–2627, J0124+0044, HE0940–1050, J1201+0116 and PKS2126–158) are quasars at the centre of an LBG field. The last column gives the approximate S/N per pixel over the Ly α forest.

Num.	Name	Field	R.A. (J2000)	Dec (J2000)	z	Resolution (km s ⁻¹)
6	LBQS 0041–2607	Q0042–2627	00:43:58.80	–25:51:15.7	2.50	120
9	LBQS 0041–2658	Q0042–2627	00:44:05.85	–26:42:04.4	2.46	120
12	LBQS 0042–2657	Q0042–2627	00:45:19.57	–26:40:50.9	2.90	120
14	LBQS 0041–2638	Q0042–2627	00:43:42.79	–26:22:10.2	3.05	120
79	Q094244.40–112138.7	HE0940–1050	09:42:44.40	–11:21:38.7	2.96	230
84	Q094342.99–105231.6	HE0940–1050	09:43:42.99	–10:52:31.6	3.01	230
96	Q094230.55–104850.8	HE0940–1050	09:42:30.55	–10:48:50.8	2.33	230
112	SDSS J120138.56+010336.1	J1201+0116	12:01:38.564	+01:03:36.22	3.84	230
141	Q213007.46–153320.9	PKS2126–158	21:30:07.460	–15:33:20.90	3.46	230

Table 6. Quasars with low resolution spectra in and around the LBG fields. Listed are all quasars that contribute to the Ly α -LBG cross-correlation for the low resolution sample shown in Fig. 13. Their spectra are shown in Fig. 10.

equivalent width of the C IV λ 1548 transition for each C IV system.

Significant absorption features were identified in a similar manner to that described by Schneider et al. (1993). The equivalent width per pixel was calculated taking into account the instrumental resolution, assumed to be a Gaussian profile. We identified all features with a minimum significance level (the ratio of the equivalent width to the equivalent width error) of four. We then scanned each spectrum by eye, searching for possible C IV systems between the quasar Ly α and C IV emission lines. For the HIRES and UVES spectra, once we identified C IV systems, we measured the total equivalent width of the C IV λ 1548 transition. We considered any C IV absorption components that were separated by less than 500 km s⁻¹ to be part of a single system. The lower resolution spectra could not resolve individual C IV components, so we fitted the candidate systems identified by eye with Gaussian profiles. We checked these fits were consistent with the relative oscillator strengths of the transitions, taking into account possible line saturation. In these lower resolution spectra we used the deblended profile for the C IV λ 1548 transition to measure a system’s equivalent width. Table C3 gives the redshifts and observed equivalent widths for C IV systems we identified towards the quasars in our sample.

5.2 C IV close to LBGs

The three LBGs in our sample closest to background sightlines have proper impact parameters of 100, 140 and 150 h^{-1} kpc. The two closest of these do not show any C IV absorption within 1000 km s⁻¹ of the LBG nebular redshift to 3σ column density detection limits of 10^{13} cm⁻² (100 kpc) and 10^{12} cm⁻² (140 kpc). For the furthest there is a probable Lyman limit system with both high (C IV, Si IV, O VI) and low (H I, O I, C II, Si II, Si III) ionization transitions ~ 500 km s⁻¹ away from the LBG redshift. The two non-detections suggest that if the C IV enveloping LBGs extends beyond ~ 100 kpc, its covering factor must be less than unity or its column density lower than 10^{13} cm⁻². The Lyman limit system could be associated with the nearby LBG, but it could also be associated with a fainter, closer galaxy that does not appear in our survey. We intend to use the large number of transitions to explore the physical conditions of this system in a future analysis (see also Simcoe et al. 2006).

5.3 C IV-LBG cross-correlation

To measure the 3-d comoving separation between an LBG and C IV system, Δs , we first find the comoving distance r to each object using

$$r = \frac{c}{H_0} \int_0^z \frac{dz'}{\sqrt{\Omega_m(1+z')^3 + \Omega_\Lambda}}, \quad (2)$$

where c is the speed of light and z is the redshift of the LBG or absorber. The separation is then given by

$$\Delta s = \sqrt{r_1^2 + r_2^2 - 2r_1r_2 \cos \theta}, \quad (3)$$

where r_1 and r_2 are the comoving distances to the LBG and absorber, and θ is their angular separation. We calculate the cross-correlation using the ratio of the number of C IV-galaxy pairs in the real data to the number for a random distribution of C IV absorbers for different separation bins. We generated a random C IV absorber catalogue in the following way: for each sightline where we measured C IV absorption, we generate $1000 \times N$ random absorbers with redshifts drawn at random between the maximum and minimum C IV redshifts able to be detected along that sight-line, where N is the number of real absorbers found along that sightline. We generated 1000 times more random absorbers to ensure the Poisson noise introduced by the number of random pairs had a negligible contribution to the final error estimate. This method assumes that the detection limits do not change significantly along a single sightline, which is a reasonable approximation for our spectra.

Fig. 11 shows the C IV-LBG correlation function as filled circles. Our C IV $\lambda 1548$ rest equivalent width distribution ranges from 0.005 to 2 Å, with a median of 0.31 Å, or $N_{\text{C IV}} = 10^{13.9} \text{ cm}^{-2}$ assuming unsaturated absorption. At separations $< 5 h^{-1} \text{ Mpc}$ A05 fitted their C IV-LBG correlation function with a function of the form $\xi(r) = (r/r_0)^{-1.6}$. They measured a clustering strength $r_0 \sim 5 h^{-1} \text{ Mpc}$ between LBGs and absorbers with $N \approx 10^{13.9} \text{ cm}^{-2}$, slightly higher than both their and our LBG-LBG r_0 values (Bielby et al. 2010). This relation is shown in Fig. 11 as a solid curve. In an attempt to increase statistical power, we measured the cross-correlation in a single bin in the range $5 - 15 h^{-1} \text{ Mpc}$. This yielded a correlation of 0.20 ± 0.16 , where we assume a 1σ Poisson error from the number of absorbers contributing to this bin. Thus the A05 relation is consistent with our measurement, but the strength is too low for us to detect the clustering signal with our sample size. We also split our sample into high and low equivalent width sub-samples to measure the clustering strength as a function of column density (solid and open triangles in Fig. 11). However, the results were inconclusive due to the small number of galaxy-C IV pairs. We are in the process of assembling a larger sample of C IV absorbers near LBGs using the X-shooter spectrograph on the VLT.

6 Ly α AUTO-CORRELATION

Before embarking on the Ly α -LBG cross-correlation we measure the Ly α flux auto-correlation along quasar sightlines in our sample, with the aim of measuring the velocity dispersion of H I gas giving rise to Ly α absorption at the redshift of our sample. As will be shown in the next section, any velocity smoothing in the redshift direction has a large effect on our ability to detect a peak in the Ly α transmissivity around LBGs. If H I gas does not share the intrinsic velocity dispersion of nearby LBGs, then its own dispersion will contribute to this velocity smoothing in the Ly α -LBG signal.

Simulations show that at $z \sim 2.5$ and at scales where linear theory holds, the Ly α forest flux auto-correlation

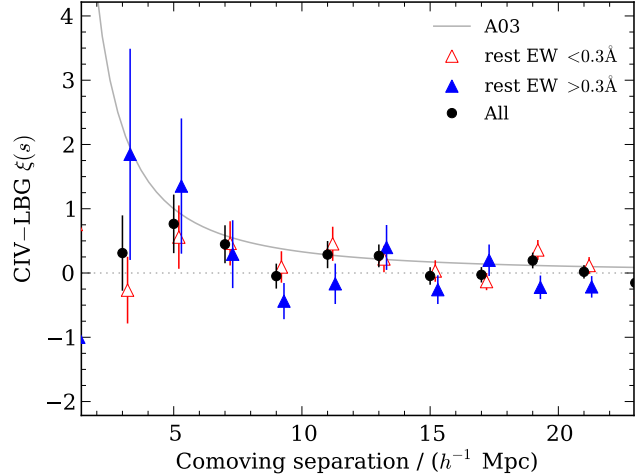


Figure 11. The cross-correlation of C IV systems with LBGs as a function of 3-d distance between the C IV absorbers and LBGs. The cross-correlation for the subsets of C IV systems with rest equivalent widths $< 0.3 \text{ Å}$ and $> 0.3 \text{ Å}$ are shown by open and filled triangles, each slightly offset for clarity. The model used in A05 to fit the C IV-LBG cross-correlation at scales $< 5 h^{-1} \text{ Mpc}$, $\xi(r) = (r/5.0)^{-1.6}$, is shown by the solid line.

function is given by the dark matter correlation function scaled by a constant and largely scale-independent factor (e.g. Croft et al. 2002; Slosar et al. 2009). By comparing the measured flux correlation function to the dark matter correlation, we can estimate the magnitude of the H I gas velocity dispersion by the size of the departure from the expected correlation function on non-linear scales.

We measure the correlation function in the following way. For each pixel in the Ly α forest region of each quasar we calculate the quantity

$$\delta = T/\bar{T} - 1, \quad (4)$$

where T is the measured transmissivity and \bar{T} is the mean transmissivity at the pixel redshift. To calculate the separation in $h^{-1} \text{ Mpc}$ between two pixels, we convert the redshift of each pixel to a comoving distance using equation 2. The correlation along the sightline is then given by

$$\xi(\Delta r) = \langle \delta(r)\delta(r + \Delta r) \rangle, \quad (5)$$

where $\langle \rangle$ denotes a sum over all pixels with a comoving separation Δr . In practice we select some finite range of separations around Δr and include all pixels with separations that fall inside that range.

Fig. 12 shows the Ly α forest flux auto-correlation from our high resolution quasar sample (resolution FWHM $\sim 7 \text{ km s}^{-1}$). We use this rather than the low resolution sample because it makes the largest contribution to the LBG-Ly α correlation at small scales, and probes the Ly α $\xi(\Delta r)$ down to $\sim 100 \text{ kpc}$ scales. We masked any DLAs or regions with poor sky subtraction in the spectra. Error bars were estimated using a jackknife technique; we calculate $\xi(\Delta r)$ seven times, each time removing a different quasar from the sample, and the error is then given by the standard deviation of these around the value from the full sample, times $(7 - 1) = 6$. We compare our results to those of Croft et al.

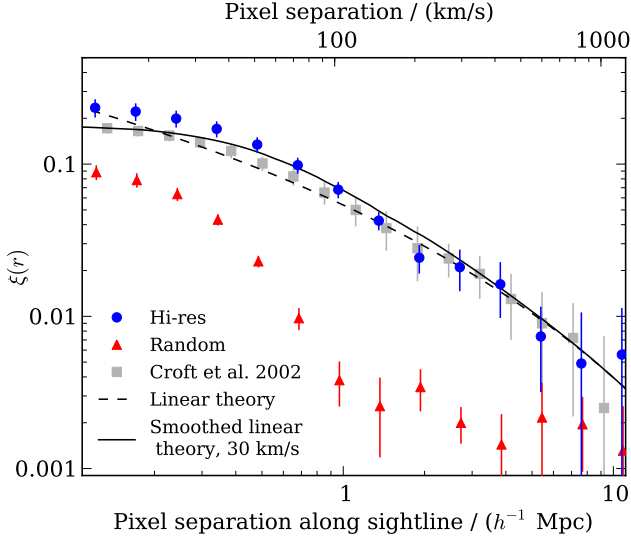


Figure 12. The auto-correlation of Ly α forest pixels along quasar sightlines for our high resolution sample. Circles show our measured auto-correlation as a function of pixel separation along the quasar sightline. Separations are given in h^{-1} Mpc (bottom) and km s^{-1} (top, using our assumed cosmology and $z = 3$). The correlation measured by Croft et al. (2002) at $z \sim 3$ are shown as pale grey squares. Triangles show the correlation measured using a set of mock spectra with thermal and instrumental broadening, but otherwise random, uncorrelated Ly α forest absorption. Also shown is the linear theory matter correlation function, convolved in the redshift direction with a Gaussian velocity distribution with FWHM 30 km s^{-1} and scaled to match the observed correlation function. The velocity dispersion of H I gas is small compared to velocity errors on the LBG positions.

(2002), who measure the auto-correlation using a sample of 30 high resolution ($\sim 8 \text{ km s}^{-1}$), high S/N spectra. Our result is slightly higher than that of Croft et al.; this is likely due to the different redshift ranges of our samples ($z \sim 3$ for the Croft et al. sample and $z \sim 3.3$ for ours).

To explore the effect of intrinsic line broadening, instrumental resolution, and incomplete wavelength coverage due to the removal of parts of spectra affect by DLAs or sky lines, we generate synthetic spectra and measure their correlation. Each synthetic spectrum has a Ly α forest generated by adding absorption lines with a redshift, b parameter and column density drawn at random from the distributions over the redshift range corresponding to an observed spectrum (see Appendix C). This sample of synthetic spectra has Ly α forest lines placed at random such that they reproduce the mean flux and b parameter distributions, which are well known from large samples of high-resolution spectra. However, the synthetic spectra do not show any correlation in absorption other than that caused by line broadening and instrumental effects. The auto-correlation for these synthetic spectra is shown in Fig. 12 by triangles. There is significant correlation at small separations, mostly due to intrinsic broadening, but past separations of 70 km s^{-1} ($\sim 0.7 h^{-1} \text{ Mpc}$) it is many times smaller than the signal from the real Ly α forest. Therefore, we believe that there are no systematic effects in our sample that introduce a spurious auto-correlation signal.

The black line in Fig. 12 shows the expected dark matter correlation function from linear theory using $\sigma_8 = 0.8$, multiplied by a factor of 0.08 and convolved with a Gaussian velocity distribution of width 30 km s^{-1} (note we did not include any contribution from gravitational infall). Much larger dispersions, $\sim 100 \text{ km s}^{-1}$, flatten $\xi(\Delta r)$ at small separations, and are not consistent with the data. We conclude that the velocity dispersion is $\sim 30 \text{ km s}^{-1}$. This is much smaller than the measured velocity dispersion of the LBGs, and so we do not consider it any further in our analysis of the LBG-Ly α cross-correlation.

7 LBG – Ly α CROSS-CORRELATION

To measure the LBG-Ly α cross-correlation we must compare the measured Ly α transmissivity close to LBGs to the mean Ly α transmissivity. The mean transmissivity in the Ly α forest decreases with increasing redshift due to evolution of the UV ionising background, structure formation, and the expansion of the Universe. This is a significant effect; from $z = 2.5$ to $z = 3.5$ the mean transmissivity drops from ~ 0.8 to ~ 0.6 . We used two methods for estimating the mean transmissivity as a function of redshift. The first uses the measured mean transmissivity from McDonald et al. (2000),

$$\bar{T} = 0.676 - 0.220(z - 3). \quad (6)$$

This is measured from the mean flux along eight quasar sightlines and was used by Adelberger et al. (2003). Over our redshift range it is very similar to the more recent result by Faucher-Giguère et al. (2008). Our second approach was to measure \bar{T} in the Ly α forest region for each individual quasar sightline. For the high resolution and low resolution samples, we used the \bar{T} estimate that gives the smallest quasar to quasar scatter in the Ly α -LBG cross correlation function. For the high resolution sample, this is the McDonald relation, and for the low resolution sample, the measured mean. For the low resolution sample, we believe the measured mean gives less scatter by compensating for errors in the inferred continuum level over the Ly α forest. At the AAOmega spectral resolution Ly α forest lines are not resolved, and line blending means that no part of a spectrum returns to the intrinsic continuum level. Thus our continuum fitting process will likely be offset from the true continuum level by 5 – 10%, and using the measured mean flux minimises the effect of such an offset.

7.1 Systematic effects

There are two issues that could affect the Ly α -LBG cross-correlation measurement. In addition to Ly α absorption, the forest region contains absorption from metal transitions. Thus there will be a small contribution to the measured transmissivity by metal absorption lines, decreasing the transmissivity below the expected mean value. However, we do not expect metal absorption at redshifts significantly different from a galaxy's redshift to correlate with the galaxy position. Therefore, we do not expect metal absorption to bias any correlation signal, instead it will tend to reduce the strength of any measured correlation.

We also cannot completely rule out a systematic offset

in our LBG redshifts. As we can only measure the redshifts for the ISM absorption lines and Ly α emission lines, which are affected by winds and H I absorption, respectively, we must infer the intrinsic redshift of the galaxies using the relation from Adelberger et al. (2005). This could introduce a systematic offset between our inferred LBG redshifts and the true redshifts, and thus an offset between the LBG positions and Ly α absorption. A more recent relation between the Ly α , ISM and intrinsic LBG redshifts is given by Steidel et al. (2010). However, this was calibrated using an LBG sample with $2 < z < 2.6$, and our LBG distribution extends to $z \sim 3.5$. Thus for our analysis we choose to use the A05 relation that was calibrated using a $2 < z < 3.5$ LBG sample. The best way to quantify any systematic redshift offsets in our sample is to obtain NIR emission lines for LBGs close to the quasar sightlines; we are pursuing such observations for LBGs where these lines are observable.

7.2 Measuring the cross-correlation

We performed the cross-correlation using the normalised quasar transmissivity profiles, $T' = T/\bar{T}$. We calculated the Ly α -LBG cross-correlation function in $0.5 h^{-1}$ Mpc bins by measuring the mean normalised transmissivity in all regions of the Ly α forest enclosed in spherical shell around each LBG with inner and outer radii given by the bin edges. The separations, s , between each Ly α pixel and an LBG were calculated using equations 2 and 3, and the bin size was chosen to match that used by A05.

The mean transmissivity in each bin was taken to be the mean of the individual transmissivity values for each LBG contributing to that bin. The errors on each bin value were taken to be the standard error in the mean of the LBG to LBG transmissivity values. We note that for points where few LBGs contribute to a bin, this will probably underestimate the error. Finally, we scaled the mean transmissivity for the Ly α forest of each quasar to 0.76 to enable a comparison with the results of A05.

7.3 Results

The VLT LBG-Ly α cross-correlation function is shown separately for the high resolution and low resolution quasar samples in Fig. 13. On scales $3 - 11 h^{-1}$ Mpc the two samples agree. There appears to be an offset between the low resolution and high resolution samples at large separations, likely due to residual continuum-fitting errors in the low-resolution spectra.

For transmissivities in the three bins with separations $< 2 h^{-1}$ Mpc, the low resolution sample increases above the mean, apparently becoming inconsistent with the high resolution sample. However, we do not believe this inconsistency is real; rather it is a result of small number statistics. In the three smallest separation bins, only four LBGs contribute to the measured transmissivities.

The LBG-Ly α cross-correlation function for the combined low and high resolution samples is shown in Fig. 14. At scales $> 2 h^{-1}$ Mpc the combined VLT result is consistent with both A03 and A05 and the relationship seems reasonably well described by a power-law, $T = 0.77 - (s/0.3 h^{-1} \text{ Mpc})^{-1}$, which also describes the A05 results (see

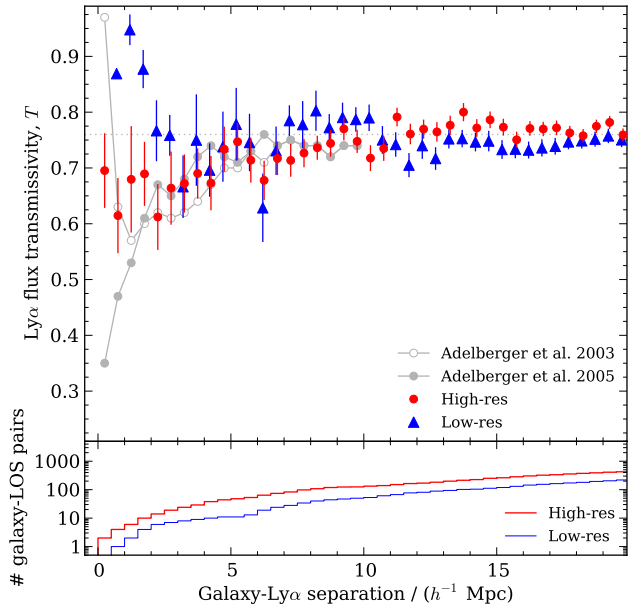


Figure 13. A comparison between the high resolution ($\sim 40,000$) and low resolution (~ 1300) quasar samples. The mean Ly α forest transmissivity in quasar spectra plotted as a function of distance from the nearest LBG. Errors are the standard error on the mean of each transmissivity measurement from a single LBG-Ly α forest region pair in a particular bin (see the discussion in the text). The results of Adelberger et al. 2003 and Adelberger et al. 2005 are also shown. The bottom panel shows the number of LBGs contributing to each bin in each sample.

Fig. 15) and the GIMIC simulation results of Tummuangpak et al. (in preparation, see also Crain et al. 2009), even at smaller scales. The VLT data aims for good statistics at large scales, so the errors are generally larger than the A03 or A05 data at smaller scales. In the case of the first point at $s = 0.25 h^{-1}$ Mpc the VLT error may be underestimated by the simple LBG-LBG error shown. In experiments where the two LBG redshifts were perturbed randomly by a velocity error drawn from a Gaussian with width 390 km s^{-1} , a larger error was obtained for this point by a factor of ≈ 3 . However, the transmissivity value is robust to changes in the estimation procedure. For example, weighting by numbers of Ly α pixels contributing to a bin rather than the number of LBGs did not significantly change this result. At the smallest scales, $s < 2 h^{-1}$ Mpc, our result lies between these two previous results, but taking the errors into account there is no significant disagreement with either. We also note that our LBG sample has a mean redshift of 3, closer to A03 than the A05 mean redshift of 2.5. Thus it is possible that evolution in the LBG-IGM relation from $z \approx 3$ to $z \approx 2.5$ explains the difference between A03 and A05 as well as the slightly better agreement of the VLT result with A03. But we suggest that statistical fluctuations remain a more likely source of any differences observed between these 3 datasets than evolution. In the next section we examine the role that LBG velocity dispersion and redshift errors play in the comparison and interpretation of these results.

7.4 Interpretation

The distance between LBGs and Ly α pixels is measured assuming we can convert velocity differences into distances, not taking into account any velocity dispersion or redshift errors. Intrinsic velocity dispersion of the LBGs and the H I gas, outflows, and LBG velocity measurement errors will thus smear out any correlation between the two along the redshift direction. Bielby et al. analysed the LBG-LBG correlation function and found it can be modelled with a real-space correlation function of $\xi(r) = (r/r_0)^{-\gamma}$ with $r_0 = 3.98 h^{-1}$ Mpc and $\gamma = 1.9$, if convolved with a pairwise velocity dispersion of $\langle w_z^2 \rangle^{1/2} = 720 \text{ km s}^{-1}$. In Section 6 we showed that the velocity dispersion of the H I gas is likely to be low, therefore we assume that the only contribution to the LBG-Ly α intrinsic velocity dispersion comes from the LBGs. For a single LBG the velocity dispersion measured by Bielby et al. is $720/\sqrt{2} = 510 \text{ km s}^{-1}$, comprising 200 km s^{-1} for the Ly α emission line outflow error and 450 km s^{-1} for the VLT VIMOS velocity measurement error, leaving 140 km s^{-1} for the intrinsic velocity dispersion.

To model the effect of this dispersion, we have taken the real-space LBG-Ly α cross-correlation function that approximately fits the A05 results and GIMIC galaxy-Ly α simulations (Tummuangpak et al., in preparation), with

$$T(s) = \bar{T} - (s/s_0)^{-1}, \quad (7)$$

where $s_0 = 0.3 h^{-1}$ Mpc. We convolved this in the redshift direction only using a velocity dispersion of 510 km s^{-1} . We do not include any contribution from infall velocities. These are not negligible (e.g. Padilla & Baugh 2002), but their contribution is likely to be small compared to the redshift uncertainties and intrinsic velocity dispersion. The result is shown in Fig. 14 by the cyan solid line. The smoothing is considerable; this is expected given that 510 km s^{-1} is $\sim 5 h^{-1}$ Mpc at $z = 3$. We have also added a central transmissivity spike to the above power-law model for $T(s)$ such that $T = 1$ for $s < 1.5 h^{-1}$ Mpc, simulating the case where high transmissivity caused by putative galactic winds are found at small scales (red solid line in Fig. 14). Both convolved results in Fig. 14 match the VLT observations. A spike of width $1.5 h^{-1}$ Mpc is wider than the sub-500 kpc spike suggested by A03's results. Thus we also consider a narrower spike of width $0.5 h^{-1}$ Mpc (red dashed line in Fig. 14). Such a spike has very little effect on the correlation function for the uncertainties on our LBG redshifts.

The original results from A03 are also affected by velocity dispersion and velocity errors, and we now estimate the correlation function that would have been measured by A03 and A05 given the models above and the redshift uncertainties of the Keck galaxy spectra. da Ângela et al. (2008) fitted a pairwise velocity dispersion of 400 km s^{-1} to the Keck LBG-LBG z -space correlation function. This converts to a dispersion of 280 km s^{-1} for a single LBG. If we assume 200 km s^{-1} for outflow error and 140 km s^{-1} for intrinsic velocity dispersion, this leaves 140 km s^{-1} velocity measurement error. 280 km s^{-1} translates to $2.8 h^{-1}$ Mpc and so it is hard to see how a narrow spike width of $0.5 h^{-1}$ Mpc seen by A03 in redshift-space could be physical. In Fig. 15 we show how such a narrow spike, shown by a green solid line, is almost smoothed away by this velocity dispersion. Even

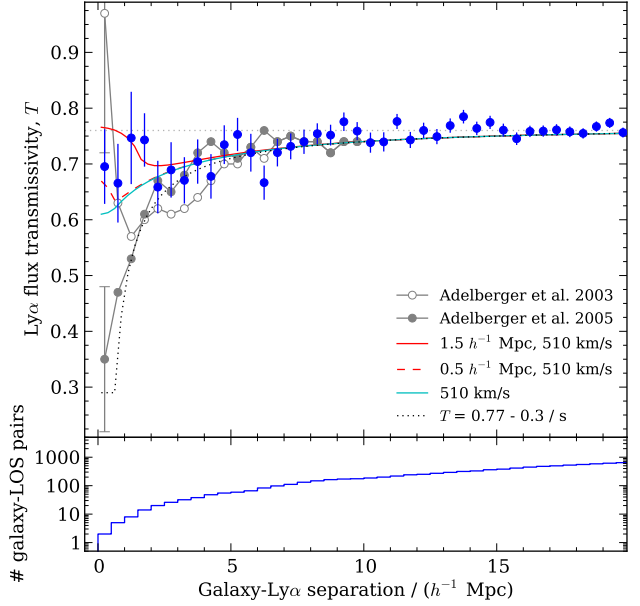


Figure 14. The mean Ly α forest transmissivity in quasar spectra plotted as a function of distance from the nearest LBG for the combined (high and low resolution) samples. We also show power law model correlation functions as described in the text. The dotted line shows the real-space power law described in the text without the effects of velocity dispersion. The cyan solid line shows this model convolved in the redshift direction with a velocity dispersion of 510 km/s , the typical uncertainty on a LBG redshift for our sample. The red lines show the power law model with a real-space $T = 1$ transmission spike at separations $< 1.5 \text{ Mpc}$ (solid) and $< 0.5 \text{ Mpc}$ (dashed), also convolved with a 510 km/s dispersion. Error bars for the values from A03 and A05 are only shown for the smallest separation point.

the NIRSPEC H_α based LBG redshifts of A05, which have 60 km s^{-1} velocity error and 140 km s^{-1} intrinsic velocity dispersion will have 150 km s^{-1} or $1.5 h^{-1}$ Mpc smoothing of the real LBG-Ly α $T(s)$. In Fig. 15 we show the effect that such a velocity dispersion has on our real-space model with (red solid line) and without (blue solid line) the narrow spike. We also show a model with a broader $1.5 h^{-1}$ Mpc spike as dashed lines for each velocity dispersion.

We conclude that at $s < 2 h^{-1}$ Mpc the VLT data could be consistent with either the existence of the $T \approx 1$ transmission spike as found by A03 or the $T \approx 0.3$ absorption found by A05. However, any $T = 1$ spike is unlikely to be as narrow as the spike originally suggested by the results of A03. The smoothing effect of even a 150 km s^{-1} velocity dispersion on a spike of width $\approx 0.5 h^{-1}$ Mpc is likely to be significant.

The velocity dispersions we are using for the Keck data could be a lower limit, since Bielby et al. find that a pairwise velocity dispersion of 700 km s^{-1} best fits the LBG-LBG redshift space, $\xi(\sigma, \pi)$, correlation function from the combined Keck LRIS and VLT data. The best estimate from the Keck LRIS data alone is similar. This would imply a much larger intrinsic pairwise LBG velocity dispersion of $\approx 600 \text{ km s}^{-1}$ and an individual LBG velocity dispersion

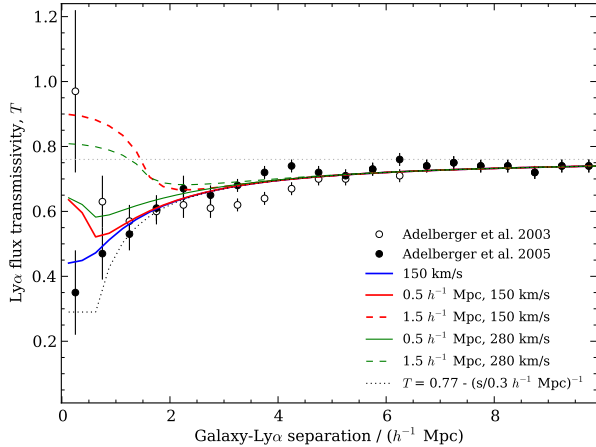


Figure 15. The mean Ly α forest transmissivity in quasar spectra plotted as a function of distance from the nearest LBG from Adelberger et al. (2003 & 2005). Also plotted are power law model correlation functions as described in the text. The dotted line shows the unconvolved power law model, and the blue line shows this model convolved with the expected uncertainty for LBGs in the NIRSPEC sample of A05. The green and red lines show models with a transmission spike of width 1.5 or 0.5 Mpc, convolved with two different velocity dispersions, as described in the text.

of $\approx 500 \text{ km s}^{-1}$. This would make the models shown in Fig. 15 to be just as appropriate for the Keck LRIS data as the VLT data, given the increasing dominance of the intrinsic dispersion. This would reinforce the conclusion that the apparent spike seen by A03 is unphysically narrow. It would also suggest the absorption feature seen by A05 has the same problem in being somewhat too narrow given the likely effect of the velocity dispersion.

Alternatively, if the absorbing H I gas has no net peculiar velocity with respect to nearby LBGs, then the contribution of the intrinsic velocity dispersion may be overestimated in the models we have presented. However, for the VLT data the measurement error is as large as any plausible intrinsic velocity dispersion, and even for the Keck data with NIRSPEC redshifts the smoothing from measurement errors alone is considerable. Thus even if LBGs and nearby H I gas share the same velocities our modelled real-space cross-correlation will not change significantly.

Despite these warnings about the effect of inter-comparing different LBG-Ly α samples with different velocity errors, we finally compare our result to the combined A05 results, constructed by taking a weighted mean of the Ly α -LBG transmissivity results for LBGs with and without NIRSPEC redshifts in A05. We compare this to the combined VLT result in Fig. 16.

Although there is excellent agreement on scales $s > 2 h^{-1} \text{ Mpc}$, the VLT data remains slightly higher than the Keck data on scales $s < 2 h^{-1} \text{ Mpc}$. This could mean that there is still a hint of feedback in the VLT result compared to the combined Keck data. However, if the individual galaxy velocity dispersions are as low as 150 km s^{-1} for the Keck (NIRSPEC) data and as high as 510 km s^{-1} for the VLT data, then both datasets may be consistent with the

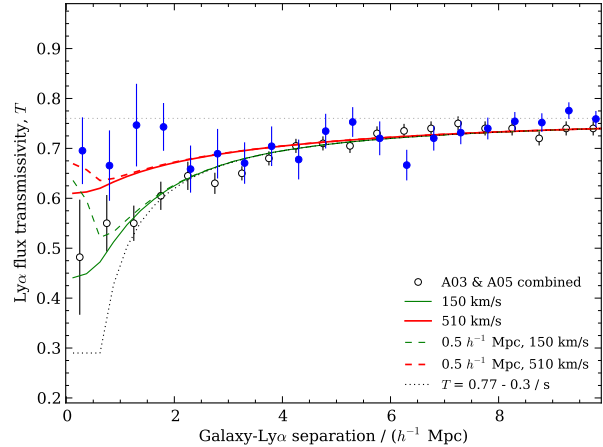


Figure 16. The mean Ly α forest transmissivity for the combined Adelberger (2005) sample, including LBGs with and without NIRSPEC redshifts, compared to our combined sample. Also plotted are power law model correlation functions as described in Fig. 14 & 15. Taking LBG velocity dispersion into account, the combined A05 results and our results are consistent with both a power law relation with no transmissivity spike, and the same relation with a narrow 0.5 Mpc transmissivity spike.

$(s/0.3 h^{-1} \text{ Mpc})^{-1}$ power law transmissivity decline (dotted line) when it is convolved with the respective velocity dispersions in the z direction (red and green solid lines). Since a $1.5 h^{-1} \text{ Mpc}$ wide, velocity convolved, transmission spike is ruled out by the Keck data alone (see Fig. 15) the only other models consistent with the data are the $0.5 h^{-1} \text{ Mpc}$ wide transmission spike models, convolved with the appropriate velocity dispersions (green and red dashed lines in Fig. 16). In both models, the transmission spike is suppressed by the velocity convolution such that they are not ruled out by either the Keck or VLT data.

We conclude that the VLT data confirms the distribution of neutral hydrogen around an LBG as indicated by the A05 results. Despite the fact that the original A03 redshift-space spike is probably unphysically narrow given the velocity effect and hence a likely statistical fluke, a narrow, real-space transmission spike is consistent with the data. Its existence would demand the presence of a high absorption region in the immediate surroundings ($s < 5 h^{-1} \text{ Mpc}$) which would disguise the spike when both are convolved with the velocity dispersion. Such an absorption region appears to be supported by both the Keck and VLT data. Models without such a $< 0.5 h^{-1} \text{ Mpc}$ spike are equally consistent with both sets of data; in this case the higher VLT result in Fig. 16 can be explained by a higher LBG velocity dispersion for the VLT data. However, a model with a $1.5 h^{-1} \text{ Mpc}$ $T = 1$ spike seems to be rejected, particularly by the Keck data.

Evidence for outflows from LBGs has also been seen in the systematic offsets between the Ly α and interstellar line redshifts (A03, A05, Bielby et al.) and so it remains of interest to improve the LBG-Ly α data to check further for the transmission spike as evidence of star-formation feedback on the IGM. In a future paper we therefore intend to

combine the full VLT and Keck LBG- $\text{Ly}\alpha$ datasets to study the LBG- $\text{Ly}\alpha$ $\xi(\sigma, \pi)$ correlation function. We can then test again for the presence of feedback by checking if any high or low spike at small scales is more clearly seen in the angular direction, where it will be less affected by velocity dispersion and redshift errors.

Spectra with better resolution and S/N for those quasars with nearby LBGs will improve the S/N of these results. We also need nebular line redshifts for LBGs near quasar lines of sight to determine better the width of any transmission spike in the VLT results at small scales. More S/N will result from the forthcoming doubling in size of our sample of VLT VIMOS LBGs in quasar survey fields. With this larger sample it will be possible to divide the LBG- $\text{Ly}\alpha$ cross-correlation function into components in the redshift and angular directions, and so search for signs of infall or outflow using anisotropies between the redshift and angular correlation functions.

8 SUMMARY

We have presented redshifts for 252 quasars across nine fields where we are surveying LBG spectroscopic redshifts with VIMOS, 164 of which are newly discovered. Using an initial sample of 1020 LBGs in five fields and 16 of our background quasars with small impact parameters from the LBGs, we have presented a measurement of the LBG- $\text{Ly}\alpha$ transmissivity and LBG-C IV cross-correlation functions. Using the 7 quasars in our sample with high-resolution spectra we have also measured the $\text{Ly}\alpha$ - $\text{Ly}\alpha$ auto-correlation function. The main results of our paper are:

- We have presented colour cuts that can be used with *ugr* imaging to select quasars in the redshift range $2.5 < z < 4$. With imaging similar to that available for Stripe 82 they yield an efficiency of 40% at a sky density of 11.2 deg^{-2} for targets to $r = 22$. With single epoch SDSS imaging, they yield an efficiency of 17% at a sky density of 4.2 deg^{-2} to $r = 21$.
- We have identified C IV absorption systems towards quasars inside the five fields where we have measured LBG redshifts. Using these systems we have measured the cross-correlation between C IV absorbers and LBGs for $5 - 15 h^{-1} \text{ Mpc}$, and find it to be consistent with the power law relation measured by Adelberger et al. (2003) at smaller separations.
- The $\text{Ly}\alpha$ auto-correlation function can be qualitatively reproduced on non-linear scales by smoothing the expected dark matter correlation function with a Gaussian velocity dispersion distribution. The width of the velocity distribution is $\sim 30 \text{ km s}^{-1}$, much smaller than the typical velocity errors on our LBG positions, and thus they do not have a significant effect on the measured $\text{Ly}\alpha$ -LBG cross-correlation.
- We have measured the $\text{Ly}\alpha$ -LBG cross-correlation for a sample of 16 background quasars with small impact parameters from foreground LBGs. The cross-correlation is consistent with the results of Adelberger et al. (2005). In particular, we also see a decrease in H I transmission at $\text{Ly}\alpha$ -LBG separations of $2 - 7 h^{-1} \text{ Mpc}$. This decrease can be described by a power law with index $\gamma = -1$.
- Uncertainties in the LBG redshifts have a significant effect on the detectability of any $\text{Ly}\alpha$ transmission spike

around the galaxies. We have examined the effect of velocity dispersion and redshift errors on the LBG- $\text{Ly}\alpha$ cross correlation using simple models of a transmission spike, and found that with the measured LBG velocity dispersions a narrow transmission spike, even if present, is difficult to measure against the underlying power law. The A03 and A05 results rule out a broad ($1.5 h^{-1} \text{ Mpc}$) transmission spike, but both their and our data are consistent with both a narrow ($0.5 h^{-1} \text{ Mpc}$) spike or no spike, once the velocity dispersion is taken into account.

In a future paper we intend to exploit our survey's wide field to analyse the $\text{Ly}\alpha$ -LBG cross-correlation function on $\sim 20 \text{ Mpc}$ scales, in both radial (redshift) and transverse directions, using a sample of ≈ 2000 LBGs.

9 ACKNOWLEDGMENTS

NC thanks the Science and Technology Facilities Council for the rolling grant that funds his position.

We thank the referee for their comments, G. Williger for providing us with electronic versions of the spectra in his paper, G. Richards for sharing photometrically selected quasar candidates from the SDSS with us and Mike Read for scanning Schmidt *U* plates for us. We also thank Paul Dobbie and Rob Sharp for their help during AAOmega observations, and advice on the use of 2DFDR. This study used data from the Keck Observatory archive and ESO archive.

This work was partially supported by the Consejo Nacional de Investigaciones Científicas y Técnicas and Secretaría de Ciencia y Técnica de la Universidad Nacional de Córdoba, and the European Union Alfa II Programme, through LENAC, the Latin American European Network for Astrophysics and Cosmology. DM, NP and LI are supported by FONDAP CFA 15010003, and BASAL CATA PFB-06.

REFERENCES

- Adelberger K. L., Shapley A. E., Steidel C. C., Pettini M., Erb D. K., Reddy N. A., 2005, *ApJ*, 629, 636
- Adelberger K. L., Steidel C. C., Shapley A. E., Pettini M., 2003, *ApJ*, 584, 45
- Baugh C. M., Lacey C. G., Frenk C. S., Granato G. L., Silva L., Bressan A., Benson A. J., Cole S., 2005, *MNRAS*, 356, 1191
- Bertin E., Arnouts S., 1996, *A&AS*, 117, 393
- Bertone S., White S. D. M., 2006, *MNRAS*, 367, 247
- Bielby R., Shanks T., Weilbacher P. M., Infante L., Crighton N. H. M., Bornancini C., Bouché N., García Lambas D., Lowenthal J., Minniti D., Padilla N., Petitjean P., Theuns T., 2010, *ArXiv e-prints*
- Bouché N., Lowenthal J. D., 2004, *ApJ*, 609, 513
- Bruscoli M., Ferrara A., Marri S., Schneider R., Maselli A., Rollinde E., Aracil B., 2003, *MNRAS*, 343, L41
- Carswell R. F., Whelan J. A. J., Smith M. G., Boksenberg A., Tytler D., 1982, *MNRAS*, 198, 91
- Covey K. R., Ivezić Ž., Schlegel D., Finkbeiner D., Padmanabhan N., Lupton R. H., Agüeros M. A., Bochanski J. J., Hawley S. L., West A. A., Seth A., Kimball A., Gogarten S. M., Claire M., Haggard D., Kaib N., Schneider D. P., Sesar B., 2007, *AJ*, 134, 2398

- Crain R. A., Theuns T., Vecchia C. D., Eke V. R., Frenk C. S., Jenkins A., Kay S. T., Peacock J. A., Pearce F. R., Schaye J., Springel V., Thomas P. A., White S. D. M., Wiersma R. P. C., 2009, *MNRAS*, 399, 1773
- Croft R. A. C., Weinberg D. H., Bolte M., Burles S., Hernquist L., Katz N., Kirkman D., Tytler D., 2002, *ApJ*, 581, 20
- da Ângela J., Shanks T., Croom S. M., Weilbacher P., Brunner R. J., Couch W. J., Miller L., Myers A. D., Nichol R. C., Pimblett K. A., de Propriis R., Richards G. T., Ross N. P., Schneider D. P., Wake D., 2008, *MNRAS*, 383, 565
- Dall'Aglio A., Wisotzki L., Worseck G., 2008, *A&A*, 480, 359
- Desjacques V., Nusser A., Haehnelt M. G., Stoehr F., 2004, *MNRAS*, 350, 879
- Fan X., 1999, *AJ*, 117, 2528
- Faucher-Giguère C., Prochaska J. X., Lidz A., Hernquist L., Zaldarriaga M., 2008, *ApJ*, 681, 831
- Frieman J. A., Bassett B., Becker A., Choi C., Cinabro D., DeJongh F., Depoy D. L., Dilday B., Doi M., Garnavich P. M., Hogan C. J., Holtzman J., Im M., Jha S., Kessler R., Konishi K., Lampeitl H., Marriner J., Marshall 2008, *AJ*, 135, 338
- Jiang L., Fan X., Cool R. J., Eisenstein D. J., Zehavi I., Richards G. T., Scranton R., Johnston D., Strauss M. A., Schneider D. P., Brinkmann J., 2006, *AJ*, 131, 2788
- Kawata D., Rauch M., 2007, *ApJ*, 663, 38
- Kim T., Cristiani S., D'Odorico S., 2001, *A&A*, 373, 757
- Kollmeier J. A., Miralda-Escudé J., Cen R., Ostriker J. P., 2006, *ApJ*, 638, 52
- Kollmeier J. A., Weinberg D. H., Davé R., Katz N., 2003, *ApJ*, 594, 75
- McDonald P., Miralda-Escudé J., Rauch M., Sargent W. L. W., Barlow T. A., Cen R., Ostriker J. P., 2000, *ApJ*, 543, 1
- Miralda-Escudé J., Cen R., Ostriker J. P., Rauch M., 1996, *ApJ*, 471, 582
- Oppenheimer B. D., Davé R., 2006, *MNRAS*, 373, 1265
- Padilla N. D., Baugh C. M., 2002, *MNRAS*, 329, 431
- Petitjean P., Webb J. K., Rauch M., Carswell R. F., Lanzetta K., 1993, *MNRAS*, 262, 499
- Pettini M., Shapley A. E., Steidel C. C., Cuby J., Dickinson M., Moorwood A. F. M., Adelberger K. L., Giavalisco M., 2001, *The ApJ*, 554, 981
- Pichon C., Vergely J. L., Rollinde E., Colombi S., Petitjean P., 2001, *MNRAS*, 326, 597
- Richards G. T., Fan X., Newberg H. J., Strauss M. A., Vanden Berk D. E., Schneider D. P., Yanny B., Boucher A., Burles S., Frieman J. A., Gunn J. E., Hall P. B., Ivezić Ž., Kent S., Loveday J., Lupton R. H., 2002, *AJ*, 123, 2945
- Richards G. T., Myers A. D., Gray A. G., Riegel R. N., Nichol R. C., Brunner R. J., Szalay A. S., Schneider D. P., Anderson S. F., 2009, *ApJS*, 180, 67
- Richards G. T., Nichol R. C., Gray A. G., Brunner R. J., Lupton R. H., Vanden Berk D. E., Chong S. S., Weinstein M. A., Schneider D. P., Anderson S. F., Munn J. A., Harris 2004, *ApJS*, 155, 257
- Saunders W., Bridges T., Gillingham P., Haynes R., Smith G. A., Whittard J. D., Churilov V., Lankshear A., Croom S., Jones D., Boshuizen C., 2004 Vol. 5492, *AAOmega: a scientific and optical overview*. pp 389–400
- Schaye J., 2001, *ApJ*, 559, 507
- Schneider D. P., Hartig G. F., Jannuzi B. T., Kirhakos S., Saxe D. H., Weymann R. J., Bahcall J. N., Bergeron J., Boksenberg A., Sargent W. L. W., Savage B. D., Turnshek D. A., Wolfe A. M., 1993, *ApJS*, 87, 45
- Sharp R., Saunders W., Smith G., Churilov V., Correll D., Dawson J., Farrel T., Frost G., Haynes R., Heald R., Lankshear A., Mayfield D., Waller L., Whittard D., 2006 Vol. 6269, *Performance of AAOmega: the AAT multipurpose fiber-fed spectrograph*. p. 14
- Simcoe R. A., Sargent W. L. W., Rauch M., Becker G., 2006, *ApJ*, 637, 648
- Slosar A., Ho S., White M., Louis T., 2009, *Journal of Cosmology and Astro-Particle Physics*, 10, 019
- Smith G. A., Saunders W., Bridges T., Churilov V., Lankshear A., Dawson J., Correll D., Waller L., Haynes R., Frost G., 2004 Vol. 5492, *AAOmega: a multipurpose fiber-fed spectrograph for the AAT*. pp 410–420
- Steidel C. C., Erb D. K., Shapley A. E., Pettini M., Reddy N. A., Bogosavljević M., Rudie G. C., Rakic O., 2010, *ArXiv e-prints*
- Steidel C. C., Giavalisco M., Pettini M., Dickinson M., Adelberger K. L., 1996, *ApJ*, 462, L17+
- Suzuki N., Tytler D., Kirkman D., O'Meara J. M., Lubin D., 2005, *ApJ*, 618, 592
- Theuns T., Viel M., Kay S., Schaye J., Carswell R. F., Tzanavaris P., 2002, *ApJ*, 578, L5
- Veilleux S., Cecil G., Bland-Hawthorn J., 2005, *ARA&A*, 43, 769
- Williger G. M., Hazard C., Baldwin J. A., McMahon R. G., 1996, *ApJS*, 104, 145
- Williger G. M., Smette A., Hazard C., Baldwin J. A., McMahon R. G., 2000, *ApJ*, 532, 77
- Wolf C., Wisotzki L., Borch A., Dye S., Kleinheinrich M., Meisenheimer K., 2003, *A&A*, 408, 499
- Worseck G., Prochaska J. X., 2010, *ArXiv e-prints*
- Worseck G., Wisotzki L., Selman F., 2008, *A&A*, 487, 539
- Young P. J., Sargent W. L. W., Boksenberg A., Carswell R. F., Whelan J. A. J., 1979, *ApJ*, 229, 891

APPENDIX A: EFFICIENCY OF QUASAR SELECTION

How can the efficiency be improved for future surveys for $2.5 < z < 4.0$ quasars? Using our quasar sample we can identify optimised colour cuts that attempt to recover a significant fraction of the available quasars while maintaining a relatively high efficiency. We use the three Stripe 82 fields for this purpose, where we have both single epoch SDSS imaging and deep Stripe 82 imaging covering the entire AAOmega fields, and we have a relatively high completeness level for quasars with $21 < r < 22$. This will allow us to determine the effect of using two different imaging depths (SDSS and Stripe 82) to select quasars.

Optimised colour cuts for SDSS imaging are shown in Fig. 2 as solid black lines. These cuts were made to recover as many of the observed $2.5 < z < 4.0$ quasars in our sample, while maintaining a high efficiency. All stellar targets with $r < 22$, and $u-g$, $g-r$ colours satisfying the optimised cuts are selected as candidates.

For Stripe 82 imaging we devised similar cuts shown by black solid lines in Fig. 3. The region between the two Stripe 82 selection polygons is not included as it is populated by A and F stars at brighter magnitudes ($r \lesssim 21$). At $r > 21$, we expect to probe past even the most distant A and F dwarfs [assuming $M_R \sim 2.1$ from Covey et al. (2007), and a maximum distance of 50 kpc; Jiang et al. (2006) also mention this point]. Thus we could in principle include this region in our selection for targets with $21 < r < 22$, but we have not done so here for simplicity.

Table A1 shows the efficiencies for the two different imaging catalogues (single epoch SDSS and Stripe 82) using the optimised cuts, and for the photo- z candidates selected from single-epoch SDSS imaging for comparison. For each selection method we define the efficiency as follows: given the total number of candidates in an AAOmega field, N_{cand} , the number of those we observed, N_{obs} , the number of candidates that were previously known to be quasars with $2.5 < z < 4.0$, N_{known} , and the number of candidates that turned out to be new quasars in the same redshift range, N_{new} , then

$$\text{efficiency} = \left(N_{\text{new}} + \frac{N_{\text{obs}}}{N_{\text{cand}}} N_{\text{known}} \right) / N_{\text{obs}}.$$

The second term inside the parentheses is required as we have observed only a subset of all the candidates, and this subset is biased by including known quasars.

Efficiencies to $R = 22$ for the Stripe 82 catalogue are around 40%, and for the single epoch SDSS imaging 13%, or 15% for photo- z selected candidates. If we extrapolate the measured efficiencies to candidates that were not observed, we expect these selection methods to yield sky densities of 11.2 quasars per deg^2 for Stripe 82, 4.0 for photo- z targets, and 9.1 for single epoch SDSS targets. This extrapolation is reasonable for the Stripe 82 and photo- z targets, but is more uncertain for the SDSS targets, as our observed candidates are highly skewed towards targets with $r < 21$. If the efficiency at $r > 21$ is much lower than that at $r < 21$ (due to larger errors in the ugr photometry, for example), then the true efficiencies and sky densities will be lower those calculated here. At $r < 21$ we have observed a large fraction of the available candidates using all the selection methods and so the extrapolation of the efficiencies is more secure. In

this case the single epoch SDSS selection efficiency is 17%, yielding a sky density of 4.2 quasars per square degree.

We conclude that it is possible to recover a sky density of $\sim 11 \text{ deg}^{-2}$ for quasars with $2.5 < z < 4$ and $R < 22$ using simple colour cuts and star/galaxy separation on imaging of a similar depth to the combined Stripe 82 catalogues, at an efficiency of $\sim 40\%$. Jiang et al. performed a similar survey for quasars using Stripe 82 imaging and they report an efficiency of 43% in the redshift range $2 < z < 3$ for targets with $g < 22.5$. This is consistent with our efficiency estimates, though over a lower redshift range and to a slightly different magnitude limit. We note that it is possible to recover higher densities: we achieved densities of $\sim 14.2 \text{ deg}^{-2}$ in the LBG areas for this redshift range, but at a much reduced efficiency of $\sim 5\%$.

APPENDIX B: GENERATING SYNTHETIC QUASAR SPECTRA

One synthetic spectrum covering the Ly α forest region was created to match each observed spectrum. For each synthetic spectrum, Ly α forest absorption was simulated by drawing many absorption lines with redshifts, b parameters and column densities drawn from the distributions observed in high resolution spectra of the Ly α forest. In generating forest lines, we follow closely the procedure of (Dall’Aglio et al. 2008). The distributions we use are as follows: for line redshifts $dn/dz \propto (1+z)^\gamma$, where $\gamma = 2.37$; for column densities $f(N_{\text{HI}}) \propto N_{\text{HI}}^{-\beta}$, where $\beta = 1.5$; and for Doppler b parameters $dn/db \propto b^{-5} \exp[-b_\sigma^4/b^4]$, where $b_\sigma = 24 \text{ km s}^{-1}$. Values for the parameters γ , β and b_σ , are taken from Kim et al. (2001), who measure them from the distribution of lines fitted to a sample of high-resolution quasar spectra.

We add forest lines to the spectrum until the mean flux in the forest region matches the measured value from McDonald et al. (2000) at the mean redshift of the forest. This flux array is then convolved with the instrumental spread function of the real spectrum. The forest absorption is multiplied by a quasar continuum generated using components derived from a principle component analysis of the continuum of low-redshift quasars (Suzuki et al. 2005). Finally we added Gaussian noise to the spectrum, varying as a function of wavelength in the same way as the real spectra.

Thus we expect the simulated spectra to reproduce the same S/N, resolution, and wavelength ranges as the observed spectra, but with uncorrelated absorption (apart from the correlations introduced by intrinsic line broadening and the instrumental broadening). We did not introduce metal lines or absorption from high column density systems (Lyman limit and damped Ly α systems) to the simulated spectra.

APPENDIX C: TABLES WITH QUASAR, DLA/LLS CANDIDATE AND CIV INFORMATION

Source	Field	Total Cand.	Obs. Cand.	Known QSOs	New QSOs	Eff.
Stripe 82, $r < 22$	J0124+0044	94	69	4	21	0.35
	Q0301-0035	92	41	8	13	0.40
	Q2348-011	79	54	8	17	0.42
	Total					0.39
SDSS <i>ugr</i> , $r < 22$	J0124+0044	233	125	2	14	0.12
	Q0301-0035	308	126	8	10	0.11
	Q2348-011	151	84	5	12	0.18
	Total					0.13
SDSS photo-z, $r < 22$	J0124+0044	85	72	3	8	0.15
	Q0301-0035	100	63	7	3	0.12
	Q2348-011	71	54	9	4	0.20
	Total					0.15
Stripe 82, $r < 21$	J0124+0044	40	31	4	10	0.42
	Q0301-0035	44	30	8	9	0.48
	Q2348-011	34	26	8	9	0.58
	Total					0.49
SDSS <i>ugr</i> , $r < 21$	J0124+0044	79	65	2	8	0.15
	Q0301-0035	115	90	7	7	0.14
	Q2348-011	44	41	5	6	0.26
	Total					0.17
SDSS photo-z, $r < 21$	J0124+0044	37	33	3	5	0.23
	Q0301-0035	49	45	6	2	0.17
	Q2348-011	39	36	9	4	0.34
	Total					0.24
SDSS <i>ugr</i> , $20 < r < 21$	J0124+0044	57	48	2	8	0.20
	Q0301-0035	84	69	4	6	0.13
	Q2348-011	31	29	3	6	0.30
	Total					0.19

Table A1. Efficiencies for selecting $2.5 < z < 4.0$ quasars for each candidate source. For all but the photo- z candidates, these are not the efficiencies we achieved in our observations, rather they are achievable efficiencies calculated using selection criteria applied after the observations. The columns show the total number of quasar candidates using the selection criteria described in Appendix A, the number of those candidates we observed, the number of candidates previously known to be quasars with $2.5 < z < 4.0$, the number of such quasars newly discovered in the observed candidates, and the efficiency as defined in Appendix A. The total efficiency for each selection method is also shown.

QUASAR SAMPLE

#	Name	Field	R.A.	Dec.	z	Mag.	O/lap?	Comments
1	[WHO91] 0042-269	Q0042-2627	00:44:52.24	-26:40:09.3	3.33	18.3	n	Wil NED $z = 3.33$
2	[WHO91] 0042-266	Q0042-2627	00:44:35.72	-26:23:00.2	2.98	19.5	y	Wil NED $z = 2.98$
3	[WHO91] 0042-267	Q0042-2627	00:45:11.33	-26:25:50.7	2.81	19.7	y	NED $z = 2.81$
4	[WHO91] 0043-259	Q0042-2627	00:46:09.67	-25:38:47.2	3.31	19.1	n	NED $z = 3.31$
5	Q0042-2627	Q0042-2627	00:44:33.95	-26:11:19.9	3.29	18.5	y	Wil NED $z = 3.289$
6	LBQS 0041-2607	Q0042-2627	00:43:58.80	-25:51:15.7	2.50	17.1	n	Wil NED $z = 2.501$
7	LBQS 0041-2707	Q0042-2627	00:43:51.84	-26:51:28.6	2.79	17.9	n	Wil NED $z = 2.786$
8	[D87] UJ3682P-038	Q0042-2627	00:46:41.65	-26:12:21.7	2.48	19.2	n	NED $z = 2.48$
9	LBQS 0041-2658	Q0042-2627	00:44:05.85	-26:42:04.4	2.46	18.6	n	Wil NED $z = 2.457$
10	[D87] UJ3682P-028	Q0042-2627	00:45:11.33	-26:58:32.1	2.34	19.8	n	Wil NED $z = 2.34$
11	[VCV96] Q 0040-2606	Q0042-2627	00:42:42.10	-25:50:09.0	2.47	19.4	n	NED $z = 2.47$
12	LBQS 0042-2657	Q0042-2627	00:45:19.57	-26:40:50.9	2.90	18.7	n	Wil NED $z = 2.898$
13	[VCV96] Q 0045-2614	Q0042-2627	00:47:45.07	-25:57:40.7	2.35	19.3	n	NED $z = 2.35$
14	LBQS 0041-2638	Q0042-2627	00:43:42.79	-26:22:10.2	3.05	18.3	y	Wil NED $z = 3.053$
16	[WHO91] 0043-265	Q0042-2627	00:45:30.47	-26:17:09.2	3.44	18.3	y	Wil NED $z = 3.44$
17	[WHO91] 0046-267	Q0042-2627	00:48:48.65	-26:27:04.1	3.52	19.7	n	NED $z = 3.52$
18	Q004340.02-260538.1	Q0042-2627	00:43:40.02	-26:05:38.1	2.20	21.5	y	VIMOS serendip.
20	Q012715.19+001828.9	J0124+0044	01:27:15.19	+00:18:28.9	2.27	21.6	n	Stripe 82
21	Q012714.65+001650.3	J0124+0044	01:27:14.65	+00:16:50.3	2.50	20.2	n	photo- $z = 2.60$
22	Q012730.08+001525.7	J0124+0044	01:27:30.08	+00:15:25.7	2.70	21.4	n	Stripe 82
23	Q012421.49+002158.3	J0124+0044	01:24:21.49	+00:21:58.3	2.94	21.8	n	Stripe 82
24	SDSS J012650.71+000933.3	J0124+0044	01:26:50.71	+00:09:33.4	3.42	20.9	n	NED $z = 3.43$
25	SDSS J012642.91+000239.0	J0124+0044	01:26:42.91	+00:02:39.0	3.22	19.7	n	NED $z = 3.23$
26	Q012617.91-000421.4	J0124+0044	01:26:17.91	-00:04:21.4	2.77	20.7	n	photo- $z = 2.44$
27	SDSS J012658.10-001202.4	J0124+0044	01:26:58.11	-00:12:02.5	2.75	20.8	n	NED $z = 2.76$
29	Q012514.44-000342.2	J0124+0044	01:25:14.44	-00:03:42.2	2.97	21.0	n	Stripe 82
30	Q012530.89-001351.8	J0124+0044	01:25:30.89	-00:13:51.8	2.58	20.6	n	SDSS
31	Q012528.25-002431.9	J0124+0044	01:25:28.25	-00:24:31.9	2.38	21.3	n	Stripe 82
32	Q012459.61-001600.7	J0124+0044	01:24:59.61	-00:16:00.7	3.15	21.0	n	Stripe 82
33	Q012429.48-000344.6	J0124+0044	01:24:29.48	-00:03:44.6	3.36	22.0	n	Stripe 82
34	Q012433.58-000335.6	J0124+0044	01:24:33.58	-00:03:35.6	2.99	21.1	n	photo- $z = 2.90$
35	Q012426.25-001708.1	J0124+0044	01:24:26.25	-00:17:08.1	2.67	21.2	n	photo- $z = 2.90$
36	Q012428.81-003835.5	J0124+0044	01:24:28.81	-00:38:35.5	2.21	21.3	n	photo- $z = 2.69$
37	Q012355.95-001853.4	J0124+0044	01:23:55.95	-00:18:53.4	3.12	20.5	n	Stripe 82
38	Q012348.47-001538.8	J0124+0044	01:23:48.47	-00:15:38.8	2.88	21.1	n	photo- $z = 2.90$
39	Q012217.48-002520.5	J0124+0044	01:22:17.48	-00:25:20.5	2.48	21.2	n	Stripe 82
40	Q012314.00-000534.4	J0124+0044	01:23:14.00	-00:05:34.4	2.53	20.5	n	photo- $z = 2.44$
41	SDSS J012114.86-001637.3	J0124+0044	01:21:14.86	-00:16:37.4	2.38	19.2	n	NED $z = 2.39$
42	Q012200.31-000308.5	J0124+0044	01:22:00.31	-00:03:08.5	2.23	21.5	n	Stripe 82
43	SDSS J012226.76+000327.5	J0124+0044	01:22:26.77	+00:03:27.5	2.47	19.7	n	NED $z = 2.48$
44	Q012145.53-000208.6	J0124+0044	01:21:45.53	-00:02:08.6	2.59	21.9	n	Stripe 82
45	Q012040.64-000947.5	J0124+0044	01:20:40.64	-00:09:47.5	2.30	21.9	n	Stripe 82
46	Q012229.58+000849.1	J0124+0044	01:22:29.58	+00:08:49.1	3.11	21.8	n	Stripe 82
47	SDSS J012039.47-000239.4	J0124+0044	01:20:39.47	-00:02:39.4	2.54	19.5	n	NED $z = 2.51$
48	SDSS J012058.06+000205.0	J0124+0044	01:20:58.07	+00:02:05.0	2.94	20.5	n	NED $z = 2.96$
49	SDSS J012019.99+000735.5	J0124+0044	01:20:20.00	+00:07:35.6	4.07	20.0	n	NED $z = 4.10$
50	Q012101.58+002102.6	J0124+0044	01:21:01.58	+00:21:02.6	2.36	20.5	n	Stripe 82
51	Q012232.22+002321.2	J0124+0044	01:22:32.22	+00:23:21.2	2.24	21.6	n	Stripe 82
52	Q012028.15+004141.9	J0124+0044	01:20:28.15	+00:41:41.9	2.97	20.6	n	photo- $z = 2.90$
53	SDSS J012052.64+004315.5	J0124+0044	01:20:52.64	+00:43:15.6	2.30	19.4	n	NED $z = 2.30$
54	Q012146.78+004645.2	J0124+0044	01:21:46.78	+00:46:45.2	2.30	20.8	n	photo- $z = 2.54$
55	Q012229.16+004039.7	J0124+0044	01:22:29.16	+00:40:39.7	2.60	21.4	n	SDSS
56	Q012203.15+010728.1	J0124+0044	01:22:03.15	+01:07:28.1	2.65	21.4	n	Stripe 82
57	Q012244.55+010604.4	J0124+0044	01:22:44.55	+01:06:04.4	2.76	21.6	n	Stripe 82
58	SDSS J012255.42+010315.3	J0124+0044	01:22:55.42	+01:03:15.4	3.46	20.8	n	NED $z = 3.51$
59	Q012351.00+005958.6	J0124+0044	01:23:51.00	+00:59:58.6	2.59	21.5	n	photo- $z = 2.79$
60	J0124+0044	J0124+0044	01:24:03.78	+00:44:32.7	3.81	17.9	y	NED $z = 3.84$

Continued on Next Page...

Table C1 – Continued

#	Name	Field	R.A.	Dec.	z	Mag.	O/lap?	Comments
61	Q012523.94+004918.6	J0124+0044	01:25:23.94	+00:49:18.6	2.46	21.9	n	Stripe 82
62	Q012552.28+005827.6	J0124+0044	01:25:52.28	+00:58:27.6	3.00	21.3	n	photo- z = 3.06
63	Q012549.03+005250.8	J0124+0044	01:25:49.03	+00:52:50.8	2.98	19.8	n	photo- z = 2.90
64	Q012434.92+002834.5	J0124+0044	01:24:34.92	+00:28:34.5	2.64	21.9	n	Stripe 82
65	Q012635.64+004532.0	J0124+0044	01:26:35.64	+00:45:32.0	2.62	21.0	n	Stripe 82
66	Q012702.83+003707.4	J0124+0044	01:27:02.83	+00:37:07.4	2.51	20.3	n	photo- z = 2.40
67	SDSS J012714.39+003249.6	J0124+0044	01:27:14.39	+00:32:49.6	2.38	20.5	n	NED z = 2.39
68	Q012558.89+002707.6	J0124+0044	01:25:58.89	+00:27:07.6	2.38	20.2	n	photo- z = 2.40
69	SDSS J012753.69+002516.4	J0124+0044	01:27:53.70	+00:25:16.4	2.45	20.7	n	NED z = 2.46
70	Q094224.73–120222.9	HE0940–1050	09:42:24.73	–12:02:22.9	2.84	19.4	n	Schmidt
71	Q094208.20–112856.7	HE0940–1050	09:42:08.20	–11:28:56.7	2.47	21.0	y	Central Imaging
72	Q094408.14–105040.0	HE0940–1050	09:44:08.14	–10:50:40.0	2.68	20.8	n	Central Imaging
73	Q094331.59–111949.3	HE0940–1050	09:43:31.59	–11:19:49.3	2.61	21.3	y	Central Imaging
76	Q094220.07–112215.9	HE0940–1050	09:42:20.07	–11:22:15.9	2.81	21.5	y	Central Imaging
77	Q093956.82–111122.6	HE0940–1050	09:39:56.82	–11:11:22.6	2.81	19.4	n	Schmidt
78	Q094446.69–113512.8	HE0940–1050	09:44:46.69	–11:35:12.8	2.82	20.7	n	Central Imaging
79	Q094244.40–112138.7	HE0940–1050	09:42:44.40	–11:21:38.7	2.96	19.6	y	WW z = 2.96
80	J0938535–105715	HE0940–1050	09:38:53.50	–10:57:15.8	2.45	17.9	n	NED z = 2.455
81	Q094349.59–112800.8	HE0940–1050	09:43:49.59	–11:28:00.8	3.48	20.7	y	Central Imaging
83	Q094053.27–111107.2	HE0940–1050	09:40:53.27	–11:11:07.2	2.46	20.4	n	Central Imaging
84	Q094342.99–105231.6	HE0940–1050	09:43:42.99	–10:52:31.6	3.01	19.6	y	WW z = 3.02
85	Q094130.12–113226.7	HE0940–1050	09:41:30.12	–11:32:26.7	3.00	20.8	n	Central Imaging
89	Q094407.71–112632.2	HE0940–1050	09:44:07.71	–11:26:32.2	2.83	19.9	y	Central Imaging
90	Q094436.51–110217.6	HE0940–1050	09:44:36.51	–11:02:17.6	2.90	21.8	n	Central Imaging
91	Q094357.66–105435.1	HE0940–1050	09:43:57.66	–10:54:35.1	3.00	20.8	n	Central Imaging
92	Q094400.94–114757.5	HE0940–1050	09:44:00.94	–11:47:57.5	2.90	19.5	n	Schmidt
93	Q094252.79–112707.6	HE0940–1050	09:42:52.79	–11:27:07.6	3.15	20.8	y	Central Imaging
94	Q094400.38–112732.7	HE0940–1050	09:44:00.38	–11:27:32.7	2.56	18.7	y	Central Imaging
95	Q094330.04–104958.7	HE0940–1050	09:43:30.04	–10:49:58.7	2.22	19.9	y	WW z = 2.22
96	Q094230.55–104850.8	HE0940–1050	09:42:30.55	–10:48:50.8	2.33	19.1	y	WW z = 2.33
98	Q094206.40–113227.3	HE0940–1050	09:42:06.40	–11:32:27.3	2.93	18.7	n	Schmidt
99	Q094446.00–113216.9	HE0940–1050	09:44:46.00	–11:32:16.9	3.00	21.7	n	Central Imaging
100	Q094324.23–105332.8	HE0940–1050	09:43:24.23	–10:53:32.8	2.76	21.4	y	WW z = 2.76
101	HE0940–1050	HE0940–1050	09:42:53.50	–11:04:25.9	3.05	16.6	y	NED z = 3.05
103	Q094253.07–110456.4	HE0940–1050	09:42:53.07	–11:04:56.4	3.79	24.7	y	VIMOS serendip.
104	2QZ J120117.1+010045	J1201+0116	12:01:17.11	+01:00:46.0	2.38	20.1	n	NED z = 2.38
105	2QZ J115948.5+003203	J1201+0116	11:59:48.61	+00:32:04.3	2.27	22.1	n	NED z = 2.27
106	Q120220.06+002242.1	J1201+0116	12:02:20.06	+00:22:42.1	2.58	17.6	n	SDSS
107	Q115840.06+014335.2	J1201+0116	11:58:40.06	+01:43:35.2	2.98	21.1	n	SDSS
108	Q120244.72+020528.5	J1201+0116	12:02:44.72	+02:05:28.5	3.52	20.3	n	SDSS
109	2QZ J120529.7+012326	J1201+0116	12:05:29.72	+01:23:26.3	2.51	20.5	n	NED z = 2.51
110	J1201+0116	J1201+0116	12:01:44.37	+01:16:11.7	3.20	17.4	y	NED z = 3.23
111	2QZ J120210.5+011543	J1201+0116	12:02:10.55	+01:15:44.3	2.50	19.9	y	NED z = 2.50
112	SDSS J120138.56+010336.1	J1201+0116	12:01:38.56	+01:03:36.2	3.84	20.1	y	NED z = 3.88
113	SDSS J115923.69+015224.2	J1201+0116	11:59:23.70	+01:52:24.0	2.44	20.1	n	NED z = 2.44
114	2QZ J120222.6+010119	J1201+0116	12:02:22.68	+01:01:20.1	2.28	20.2	n	NED z = 2.28
115	2QZ J120055.7+013430	J1201+0116	12:00:55.77	+01:34:30.8	2.51	20.6	n	NED z = 2.51
116	2QZ J115949.8+004329	J1201+0116	11:59:49.84	+00:43:29.6	2.71	20.0	n	NED z = 2.71
118	Q120408.38+014507.5	J1201+0116	12:04:08.38	+01:45:07.5	2.30	20.7	n	Photo- z = 2.325
119	2QZ J120148.0+002000	J1201+0116	12:01:48.04	+00:20:00.8	2.83	20.4	n	NED z = 2.83
120	2QZ J120311.2+015209	J1201+0116	12:03:11.30	+01:52:09.9	2.27	20.2	n	NED z = 2.27
121	SDSS J120045.05+013953.3	J1201+0116	12:00:45.06	+01:39:53.2	2.23	19.2	n	NED z = 2.23
122	Q120001.29+003432.7	J1201+0116	12:00:01.29	+00:34:32.7	3.36	20.0	n	SDSS
123	Q120034.67+011518.4	J1201+0116	12:00:34.67	+01:15:18.4	2.62	24.2	y	VIMOS serendip.
124	Q120123.83+012115.7	J1201+0116	12:01:23.83	+01:21:15.7	2.73	24.3	y	VIMOS serendip.
125	Q120104.76+012213.8	J1201+0116	12:01:04.76	+01:22:13.8	2.91	22.8	y	VIMOS serendip.
126	Q120219.73+012534.8	J1201+0116	12:02:19.73	+01:25:34.8	2.53	23.0	y	VIMOS serendip.

Continued on Next Page...

Table C1 – Continued

#	Name	Field	R.A.	Dec.	z	Mag.	O/lap?	Comments
127	Q120139.01+011733.9	J1201+0116	12:01:39.01	+01:17:33.9	3.73	21.6	y	VIMOS serendip.
128	Q213144.16–155746.4	PKS2126–158	21:31:44.16	–15:57:46.4	3.86	18.4	n	Schmidt
129	Q213141.42–160231.5	PKS2126–158	21:31:41.42	–16:02:31.5	2.14	18.2	n	Schmidt
130	Q213054.40–160540.4	PKS2126–158	21:30:54.40	–16:05:40.4	2.58	19.8	n	Schmidt
131	Q212904.90–160249.0	PKS2126–158	21:29:04.90	–16:02:49.0	2.90	19.2	n	Schmidt
132	Q212719.00–161001.1	PKS2126–158	21:27:19.00	–16:10:01.1	2.54	19.7	n	Schmidt
134	PKS2126–158	PKS2126–158	21:29:12.15	–15:38:40.9	3.27	17.3	y	NED $z = 3.26$
135	Q212658.46–150839.8	PKS2126–158	21:26:58.46	–15:08:39.8	2.19	20.2	n	Schmidt
136	Q212732.20–151026.6	PKS2126–158	21:27:32.20	–15:10:26.6	2.29	19.8	n	Schmidt
138	Q212910.85–152423.7	PKS2126–158	21:29:10.85	–15:24:23.7	2.43	20.3	y	WW $z = 2.480$
139	Q212916.60–144542.6	PKS2126–158	21:29:16.60	–14:45:42.6	2.32	20.0	n	Schmidt
140	Q212922.08–150653.2	PKS2126–158	21:29:22.08	–15:06:53.2	2.40	18.6	n	Schmidt
141	Q213007.46–153320.9	PKS2126–158	21:30:07.46	–15:33:20.9	3.46	21.9	y	WW $z = 3.487$
142	Q213201.80–153256.4	PKS2126–158	21:32:01.80	–15:32:56.4	2.74	17.8	n	Schmidt
143	Q212920.40–153816.1	PKS2126–158	21:29:20.40	–15:38:16.1	3.81	23.4	y	VIMOS serendip.
145	Q212812.15–154533.0	PKS2126–158	21:28:12.15	–15:45:33.0	3.64	22.8	y	VIMOS serendip.
146	Q212814.66–155338.6	PKS2126–158	21:28:14.66	–15:53:38.6	3.17	22.7	y	VIMOS serendip.
147	Q223732.18–001730.6	Q2231–0015	22:37:32.18	–00:17:30.6	2.57	19.5	n	SDSS
148	Q223450.81–001743.1	Q2231–0015	22:34:50.81	–00:17:43.1	2.80	21.1	n	SDSS
149	Q223427.19–001419.9	Q2231–0015	22:34:27.19	–00:14:19.9	2.90	21.8	n	Central Imaging
150	SDSS J223421.08–004800.5	Q2231–0015	22:34:21.09	–00:48:00.5	3.02	19.9	n	NED $z = 3.02$
151	SDSS J223359.82–005841.0	Q2231–0015	22:33:59.82	–00:58:41.0	2.41	19.7	n	NED $z = 2.41$
152	Q223315.39–003146.5	Q2231–0015	22:33:15.39	–00:31:46.5	2.79	20.3	n	SDSS
153	SDSS J223250.37–004623.9	Q2231–0015	22:32:50.38	–00:46:24.0	2.39	19.8	n	NED $z = 2.39$
154	Q223334.36–000541.2	Q2231–0015	22:33:34.36	–00:05:41.2	2.47	21.9	y	Central Imaging
155	SDSS J223118.34–003321.4	Q2231–0015	22:31:18.35	–00:33:21.4	2.52	19.2	n	NED $z = 2.52$
156	Q223256.67–001246.4	Q2231–0015	22:32:56.67	–00:12:46.4	3.10	21.8	n	Central Imaging
157	SDSS J223253.56–001119.4	Q2231–0015	22:32:53.57	–00:11:19.4	3.11	20.2	n	NED $z = 3.11$
158	SDSS J223438.52+005730.0	Q2231–0015	22:34:38.52	+00:57:30.0	2.85	19.2	n	NED $z = 2.85$
159	SDSS J223433.70+002846.9	Q2231–0015	22:34:33.71	+00:28:47.0	2.74	20.9	n	NED $z = 2.74$
160	SDSS J223535.59+003602.0	Q2231–0015	22:35:35.59	+00:36:02.1	3.87	20.4	n	NED $z = 3.87$
161	SDSS J223502.19+002141.8	Q2231–0015	22:35:02.20	+00:21:41.8	3.27	20.5	n	NED $z = 3.27$
162	Q2231–0015	Q2231–0015	22:34:09.00	+00:00:01.7	3.02	17.3	y	NED $z = 3.02$
163	Q223440.85+000647.7	Q2231–0015	22:34:40.85	+00:06:47.7	2.47	21.8	y	Central Imaging
164	Q223706.63+002413.4	Q2231–0015	22:37:06.63	+00:24:13.4	2.66	21.5	n	SDSS
165	SDSS J223716.03+001914.5	Q2231–0015	22:37:16.03	+00:19:14.5	2.51	18.7	n	NED $z = 2.51$
166	Q223515.41+000519.7	Q2231–0015	22:35:15.41	+00:05:19.7	2.72	19.5	n	SDSS
167	SDSS J235420.60–003534.0	Q2348–011	23:54:20.60	–00:35:34.0	3.15	20.3	n	NED $z = 3.14$
169	Q235400.37–004203.5	Q2348–011	23:54:00.37	–00:42:03.5	2.36	20.5	n	photo- $z = 2.46$
170	Q235234.52–004006.1	Q2348–011	23:52:34.52	–00:40:06.1	2.66	21.1	n	SDSS
171	Q235351.86–004416.1	Q2348–011	23:53:51.86	–00:44:16.1	2.82	20.2	n	photo- $z = 2.75$
172	SDSS J235344.85–004621.5	Q2348–011	23:53:44.85	–00:46:21.5	2.23	19.8	n	NED $z = 2.23$
173	Q235343.09–004904.3	Q2348–011	23:53:43.09	–00:49:04.3	2.29	21.3	n	Stripe 82
174	Q235416.34–005808.3	Q2348–011	23:54:16.34	–00:58:08.3	2.49	20.6	n	SDSS
175	Q235252.99–005132.7	Q2348–011	23:52:52.99	–00:51:32.7	2.48	21.2	n	SDSS
176	SDSS J235213.08–004607.7	Q2348–011	23:52:13.08	–00:46:07.8	2.35	20.3	y	NED $z = 2.33$
177	SDSS J235206.44–004606.6	Q2348–011	23:52:06.44	–00:46:06.6	2.73	20.7	y	NED $z = 2.76$
178	Q235253.41–011752.3	Q2348–011	23:52:53.41	–01:17:52.3	3.60	21.4	n	Central Imaging
179	Q235213.16–011209.7	Q2348–011	23:52:13.16	–01:12:09.7	3.26	20.9	n	Central Imaging
180	Q235141.42–005127.4	Q2348–011	23:51:41.42	–00:51:27.4	2.16	19.6	y	Central Imaging
181	Q235201.36–011408.2	Q2348–011	23:52:01.36	–01:14:08.2	3.12	20.4	y	SDSS
182	Q235147.40–011955.7	Q2348–011	23:51:47.40	–01:19:55.7	3.50	21.7	n	Central Imaging
183	Q235119.94–011004.4	Q2348–011	23:51:19.94	–01:10:04.4	2.14	21.9	y	Stripe 82
184	Q235119.47–011229.2	Q2348–011	23:51:19.47	–01:12:29.2	2.94	20.1	y	SDSS
185	UM 184	Q2348–011	23:50:57.88	–00:52:09.9	3.01	18.7	y	NED $z = 3.02$
186	SDSS J235053.54–004810.2	Q2348–011	23:50:53.55	–00:48:10.2	3.85	19.6	y	NED $z = 3.85$
187	Q234946.70–012159.7	Q2348–011	23:49:46.70	–01:21:59.7	2.80	21.6	n	Central Imaging

Continued on Next Page...

Table C1 – Continued

#	Name	Field	R.A.	Dec.	z	Mag.	O/lap?	Comments
188	Q235029.07–005134.8	Q2348–011	23:50:29.07	–00:51:34.8	2.51	21.8	y	Stripe 82
189	Q234910.97–012046.9	Q2348–011	23:49:10.97	–01:20:46.9	3.27	21.7	n	Central Imaging
190	Q234901.15–012002.0	Q2348–011	23:49:01.15	–01:20:02.0	2.73	21.1	n	Central Imaging
191	Q234919.94–010727.0	Q2348–011	23:49:19.94	–01:07:27.0	2.75	20.8	y	SDSS
192	SDSS J235002.78–005332.9	Q2348–011	23:50:02.78	–00:53:33.0	2.44	19.0	y	NED $z = 2.41$
193	SDSS J234921.56–005915.1	Q2348–011	23:49:21.56	–00:59:15.2	3.09	19.9	y	NED $z = 3.11$
194	Q234906.09–010245.8	Q2348–011	23:49:06.09	–01:02:45.8	2.89	21.6	y	Central Imaging
195	Q234732.98–010451.6	Q2348–011	23:47:32.98	–01:04:51.6	2.40	21.8	n	Stripe 82
196	Q234958.23–004426.4	Q2348–011	23:49:58.23	–00:44:26.4	2.58	21.0	y	Central Imaging
197	Q234801.41–005532.4	Q2348–011	23:48:01.41	–00:55:32.4	2.62	20.5	n	photo- $z = 2.48$
198	Q235025.07–003838.1	Q2348–011	23:50:25.07	–00:38:38.1	2.73	21.3	y	Central Imaging
199	Q234719.09–005750.2	Q2348–011	23:47:19.09	–00:57:50.2	3.09	21.3	n	SDSS
200	Q234730.76–005131.5	Q2348–011	23:47:30.76	–00:51:31.5	2.62	20.1	n	SDSS
201	Q234712.10–004620.2	Q2348–011	23:47:12.10	–00:46:20.2	2.58	21.7	n	Stripe 82
203	SDSS J234850.78–003429.4	Q2348–011	23:48:50.79	–00:34:29.5	3.97	20.5	n	NED $z = 4.01$
205	Q234758.67–002533.2	Q2348–011	23:47:58.67	–00:25:33.2	3.03	21.9	n	Stripe 82
206	SDSS J234932.30–002614.3	Q2348–011	23:49:32.31	–00:26:14.4	2.50	20.8	n	NED $z = 2.17$
207	Q234728.48–001458.1	Q2348–011	23:47:28.48	–00:14:58.1	2.63	21.4	n	SDSS
209	Q234830.27–000935.5	Q2348–011	23:48:30.27	–00:09:35.5	2.21	21.4	n	Stripe 82
210	Q234754.57–000036.0	Q2348–011	23:47:54.57	–00:00:36.0	2.42	21.1	n	Stripe 82
211	Q234823.34+000437.8	Q2348–011	23:48:23.34	+00:04:37.8	2.66	20.9	n	photo- $z = 2.44$
212	Q235017.53–002230.6	Q2348–011	23:50:17.53	–00:22:30.6	2.51	21.7	n	Central Imaging
213	Q234911.97–000012.5	Q2348–011	23:49:11.97	–00:00:12.5	2.93	21.2	n	photo- $z = 2.40$
214	Q234902.85+001243.1	Q2348–011	23:49:02.85	+00:12:43.1	2.27	21.4	n	Stripe 82
215	Q235023.60–001958.6	Q2348–011	23:50:23.60	–00:19:58.6	2.24	21.6	n	Stripe 82
216	Q234916.38+002011.2	Q2348–011	23:49:16.38	+00:20:11.2	3.42	20.9	n	SDSS
217	Q2348–011	Q2348–011	23:51:10.82	+00:02:21.2	3.50	18.8	n	NED $z = 3.53$
218	Q235125.93+001306.6	Q2348–011	23:51:25.93	+00:13:06.6	2.71	20.8	n	photo- $z = 2.54$
219	Q235109.53–000101.6	Q2348–011	23:51:09.53	–00:01:01.6	3.12	20.8	n	SDSS
220	Q235142.12+000653.6	Q2348–011	23:51:42.12	+00:06:53.6	3.04	21.3	n	SDSS
221	Q235220.25+001735.9	Q2348–011	23:52:20.25	+00:17:35.9	3.33	21.6	n	Stripe 82
222	SDSS J235251.66+001746.6	Q2348–011	23:52:51.66	+00:17:46.6	2.53	20.4	n	NED $z = 2.33$
223	SDSS J235230.16+000552.0	Q2348–011	23:52:30.16	+00:05:52.1	3.14	20.1	n	NED $z = 3.15$
224	SDSS J235219.08–000012.1	Q2348–011	23:52:19.09	–00:00:12.1	3.42	20.3	n	NED $z = 3.43$
225	Q235259.02+000142.5	Q2348–011	23:52:59.02	+00:01:42.5	2.18	20.8	n	SDSS
226	SDSS J235224.13–000951.0	Q2348–011	23:52:24.14	–00:09:51.0	2.73	19.5	n	NED $z = 2.74$
227	Q235136.89–002429.8	Q2348–011	23:51:36.89	–00:24:29.8	2.33	21.9	n	Stripe 82
228	Q235416.52–001233.6	Q2348–011	23:54:16.52	–00:12:33.6	3.21	20.5	n	SDSS
229	Q235112.66–003124.8	Q2348–011	23:51:12.66	–00:31:24.8	2.49	21.4	y	Central Imaging
230	SDSS J235406.31–002110.5	Q2348–011	23:54:06.31	–00:21:10.6	3.52	20.4	n	NED $z = 3.54$
232	Q000258.98+070318.4	Q2359+0653	00:02:58.98	+07:03:18.4	2.72	20.9	n	Central Imaging
233	Q2359+068	Q2359+0653	00:01:40.60	+07:09:54.0	3.23	18.4	y	NED $z = 3.23$
236	Q000033.06+070716.1	Q2359+0653	00:00:33.06	+07:07:16.1	2.86	19.6	n	Central Imaging
237	Q000059.34+070900.3	Q2359+0653	00:00:59.34	+07:09:00.3	2.42	19.7	y	Central Imaging
239	Q000127.48+071911.8	Q2359+0653	00:01:27.48	+07:19:11.8	2.87	20.7	y	Central Imaging
240	Q000123.13+071559.1	Q2359+0653	00:01:23.13	+07:15:59.1	2.33	22.0	y	Central Imaging
241	Q000035.31+072503.1	Q2359+0653	00:00:35.31	+07:25:03.1	2.54	20.6	n	Central Imaging
244	Q000134.45+072312.9	Q2359+0653	00:01:34.45	+07:23:12.9	2.40	19.4	y	Central Imaging
245	Q000130.89+080536.8	Q2359+0653	00:01:30.89	+08:05:36.8	2.18	18.9	n	Central Imaging
246	Q000200.30+072636.8	Q2359+0653	00:02:00.30	+07:26:36.8	2.88	20.0	n	Central Imaging
247	Q000137.67+071412.2	Q2359+0653	00:01:37.67	+07:14:12.2	2.99	20.8	y	Central Imaging
248	Q000234.97+071349.3	Q2359+0653	00:02:34.97	+07:13:49.3	2.60	20.6	y	Central Imaging
249	Q030512.26–002727.8	Q0301–0035	03:05:12.26	–00:27:27.8	2.58	21.5	n	Stripe 82
250	SDSS J030707.09–004901.5	Q0301–0035	03:07:07.10	–00:49:01.5	3.18	20.6	n	NED $z = 3.18$
251	Q030622.41–004720.1	Q0301–0035	03:06:22.41	–00:47:20.1	2.31	21.0	n	photo- $z = 2.31$
252	Q030542.94–004058.5	Q0301–0035	03:05:42.94	–00:40:58.5	2.71	21.3	n	SDSS
253	Q030536.21–010218.0	Q0301–0035	03:05:36.21	–01:02:18.0	2.96	21.8	n	Stripe 82

Continued on Next Page...

Table C1 – Continued

#	Name	Field	R.A.	Dec.	z	Mag.	O/lap?	Comments
254	SDSS J030543.44–010622.1	Q0301–0035	03:05:43.45	–01:06:22.2	2.85	20.2	n	NED $z = 2.85$
255	Q030335.03–003247.9	Q0301–0035	03:03:35.03	–00:32:47.9	2.49	21.1	n	Central Imaging
256	Q030504.18–010522.1	Q0301–0035	03:05:04.18	–01:05:22.1	2.92	21.9	n	Stripe 82
257	SDSS J030437.56–011452.9	Q0301–0035	03:04:37.57	–01:14:53.0	2.42	19.8	n	NED $z = 2.42$
258	Q030340.93–003540.7	Q0301–0035	03:03:40.93	–00:35:40.7	2.62	21.7	n	Central Imaging
259	Q030335.09–011235.7	Q0301–0035	03:03:35.09	–01:12:35.7	3.78	21.4	n	photo- $z = 3.10$
261	Q030244.18–003817.5	Q0301–0035	03:02:44.18	–00:38:17.5	2.98	19.8	n	SDSS
262	Q030210.01–005823.0	Q0301–0035	03:02:10.01	–00:58:23.0	2.74	20.9	n	SDSS
263	SDSS J030201.51–005833.5	Q0301–0035	03:02:01.51	–00:58:33.5	2.46	20.1	n	NED $z = 2.46$
264	Q0301–0035	Q0301–0035	03:03:41.05	–00:23:21.9	3.23	17.6	y	NED $z = 3.23$
265	Q030252.20–002852.3	Q0301–0035	03:02:52.20	–00:28:52.3	2.23	20.1	n	SDSS
266	Q030241.61–002713.6	Q0301–0035	03:02:41.61	–00:27:13.6	2.81	20.1	n	Central Imaging
267	SDSS J030054.53–003403.3	Q0301–0035	03:00:54.53	–00:34:03.4	2.49	21.1	n	NED $z = 2.49$
268	SDSS J030232.00–002734.1	Q0301–0035	03:02:32.00	–00:27:34.2	2.40	19.3	n	NED $z = 2.40$
269	SDSS J030054.61–003051.8	Q0301–0035	03:00:54.61	–00:30:51.8	2.31	19.9	n	NED $z = 2.31$
270	Q030111.16–002800.4	Q0301–0035	03:01:11.16	–00:28:00.4	2.48	20.3	n	photo- $z = 2.40$
271	Q030017.55–002258.7	Q0301–0035	03:00:17.55	–00:22:58.7	2.16	21.4	n	SDSS
272	Q025948.03–001749.6	Q0301–0035	02:59:48.03	–00:17:49.6	2.56	21.9	n	Stripe 82
273	Q025959.18–001156.7	Q0301–0035	02:59:59.18	–00:11:56.7	2.15	21.4	n	Stripe 82
274	SDSS J025949.14–000825.1	Q0301–0035	02:59:49.15	–00:08:25.1	2.65	20.7	n	NED $z = 2.65$
275	Q030036.17–000549.4	Q0301–0035	03:00:36.17	–00:05:49.4	2.60	21.1	n	photo- $z = 2.31$
276	Q030254.04–001637.4	Q0301–0035	03:02:54.04	–00:16:37.4	3.00	20.2	n	SDSS
277	Q030127.86–000307.0	Q0301–0035	03:01:27.86	–00:03:07.0	2.23	21.2	n	Stripe 82
278	Q030031.52+001143.8	Q0301–0035	03:00:31.52	+00:11:43.8	2.20	21.2	n	photo- $z = 2.31$
279	Q030124.12+000445.4	Q0301–0035	03:01:24.12	+00:04:45.4	2.60	20.9	n	photo- $z = 2.44$
280	Q030109.02+001013.8	Q0301–0035	03:01:09.02	+00:10:13.8	3.01	20.5	n	photo- $z = 2.90$
281	Q030151.92+000558.5	Q0301–0035	03:01:51.92	+00:05:58.5	2.87	20.6	n	SDSS
282	Q030131.79+001514.0	Q0301–0035	03:01:31.79	+00:15:14.0	2.66	20.4	n	SDSS
283	Q030259.87–000915.4	Q0301–0035	03:02:59.87	–00:09:15.4	3.39	21.9	n	Central Imaging
284	SDSS J030222.08+000631.0	Q0301–0035	03:02:22.09	+00:06:31.1	3.33	20.8	n	NED $z = 3.33$
285	Q030324.69–001231.4	Q0301–0035	03:03:24.69	–00:12:31.4	2.72	20.6	n	Central Imaging
286	SDSS J030335.42–002001.1	Q0301–0035	03:03:35.45	–00:20:01.1	2.72	19.9	n	NED $z = 2.72$
287	Q030211.38+002228.6	Q0301–0035	03:02:11.38	+00:22:28.6	2.79	21.1	n	photo- $z = 2.90$
288	Q030437.88+002100.8	Q0301–0035	03:04:37.88	+00:21:00.8	2.93	20.3	n	SDSS
289	Q030433.52+001601.1	Q0301–0035	03:04:33.52	+00:16:01.1	2.36	21.7	n	Stripe 82
290	SDSS J030435.32–000251.0	Q0301–0035	03:04:35.33	–00:02:51.0	3.05	20.3	n	NED $z = 3.05$
291	Q030558.72+002529.3	Q0301–0035	03:05:58.72	+00:25:29.3	2.47	21.8	n	Stripe 82
292	WW2006 B	Q0301–0035	03:05:16.96	+00:00:43.5	2.81	21.3	n	WW
293	Q030506.79–000049.7	Q0301–0035	03:05:06.79	–00:00:49.7	3.04	21.9	n	Stripe 82
294	LBQS 0302–0019	Q0301–0035	03:04:49.86	–00:08:13.5	3.29	17.5	y	NED $z = 3.29$
295	SDSS J030505.90–000616.5	Q0301–0035	03:05:05.90	–00:06:16.5	3.45	20.8	n	NED $z = 3.45$
296	Q030515.60–001614.2	Q0301–0035	03:05:15.60	–00:16:14.2	2.29	19.9	n	WW
297	SDSS J030707.45–001601.4	Q0301–0035	03:07:07.46	–00:16:01.4	3.70	20.1	n	NED $z = 3.70$

Table C1: Quasars with $z > 2.1$ for which we have obtained AAOmega spectra. Coordinates are in J2000, and magnitudes are R band. The second last column indicates whether the quasar overlaps the LBG survey fields. The final comments field shows the manner in which the quasar was selected. The abbreviations in the comments field are: Wil – A spectrum for this quasar was available from Williger et al. (1996); NED – selected from the NED database; VIMOS serendip. – discovered in our VIMOS LBG observations; Stripe 82 – selected using Stripe 82 imaging; photo- z – this quasar was a candidate with a photometric redshift from Richards et al. (2004, 2009); SDSS – selected using single epoch SDSS imaging; Schmidt – selected using Schmidt plate imaging; Central Imaging – selected using the central imaging described in Table 2; WW – taken from (Worseck et al. 2008);

Num	Name	z_{qso}	Mag.	Max. $N_{\text{H I}}$	z_{abs}	Metals
16	[WHO91] 0043–265	3.44	18.3	19.8	2.817	C IV, Fe II, Al II
25	SDSS J012642.91+000239.0	3.22	19.7	20.7	2.886	C IV, Fe II
35	Q012426.25–001708.1	2.67	21.2	19.3	2.682	C IV, Si IV, Si II
37	Q012355.95–001853.4	3.12	20.5	19.7	2.880	C IV, C II
38	Q012348.47–001538.8	2.88	21.1	19.8	2.822	C IV, Si II, Si III
59	Q012351.00+005958.6	2.59	21.5	19.9	2.510	C IV, Si IV
70	Q094224.73–120222.9	2.84	19.4	20.0	2.498	C IV, Si IV, Al II
72	Q094408.14–105040.0	2.68	20.8	20.0	2.255	C IV, Al II
91	Q094357.66–105435.1	3.00	20.8	19.9	3.020	C IV, Si IV, Si II, Al II
92	Q094400.94–114757.5	2.90	19.5	20.5	2.821	C II, Al II
108	Q120244.72+020528.5	3.52	20.3	19.2	3.537	C IV, Si IV
122	Q120001.29+003432.7	3.36	20.0	19.2	3.267	C IV, Si IV
131	Q212904.90–160249.0	2.90	19.2	19.7	2.162	C IV, Si IV, Fe II, Al II
141	Q213007.46–153320.9	3.46	21.9	19.4	3.267	C IV, Si IV
141	Q213007.46–153320.9	3.46	21.9	19.1	3.478	C IV, Si IV
142	Q213201.80–153256.4	2.74	17.8	19.8	2.338	C IV, Si IV, Fe II

Table C2. DLA and LLS candidates towards low-resolution quasars in our first five LBG fields. Columns show the quasar number, name, emission redshift and magnitude from Table C1, a 1σ upper limit on the candidate system's column density (estimated using a Voigt profile with a single component of velocity width $b = 50 \text{ km s}^{-1}$), the absorber redshift and associated metals. Candidates were selected by eye, and were required to have strong H I absorption with detectable absorption from two or more associated metal transitions.

C IV SAMPLE

#	Field	quasar #	z_{qso}	z_{abs}	σz_{abs}	EW	σ EW
1	HE0940–1050	95	2.22	1.58144	0.00022	2.157	0.065
2	HE0940–1050	95	2.22	2.19780	0.00026	0.952	0.029
3	HE0940–1050	98	2.93	2.42767	0.00016	1.401	0.010
4	HE0940–1050	70	2.84	2.49789	0.00009	5.073	0.029
5	HE0940–1050	79	2.96	2.48853	0.00021	2.670	0.060
6	HE0940–1050	79	2.96	2.89225	0.00009	2.587	0.006
7	HE0940–1050	92	2.90	2.21464	0.00020	1.335	0.019
8	HE0940–1050	81	3.48	2.56623	0.00014	4.665	0.077
9	HE0940–1050	81	3.48	2.57830	0.00022	2.652	0.079
10	HE0940–1050	81	3.48	3.13576	0.00026	2.440	0.045
11	HE0940–1050	96	2.33	1.85485	0.00028	0.923	0.030
12	HE0940–1050	96	2.33	2.32154	0.00040	0.510	0.013
13	HE0940–1050	94	2.56	1.86486	0.00033	0.344	0.005
14	HE0940–1050	94	2.56	1.88062	0.00032	0.658	0.006
15	HE0940–1050	94	2.56	1.94750	0.00015	1.322	0.009
16	HE0940–1050	94	2.56	2.18651	0.00016	0.932	0.006
17	HE0940–1050	94	2.56	2.34047	0.00017	0.841	0.007
18	HE0940–1050	72	2.68	2.25497	0.00037	2.033	0.118
19	HE0940–1050	93	3.15	2.97584	0.00014	3.904	0.030
20	HE0940–1050	93	3.15	3.12947	0.00026	1.035	0.010
21	HE0940–1050	89	2.83	2.81193	0.00048	1.717	0.023
22	HE0940–1050	89	2.83	2.82790	0.00011	0.968	0.002
23	HE0940–1050	80	2.45	2.34028	0.00024	1.389	0.046
24	HE0940–1050	101	3.05	2.22093	0.00005	0.992	0.005
25	HE0940–1050	101	3.05	2.33003	0.00005	3.062	0.006
26	HE0940–1050	101	3.05	2.40893	0.00005	0.358	0.004
27	HE0940–1050	101	3.05	2.51662	0.00005	0.083	0.007
28	HE0940–1050	101	3.05	2.61360	0.00005	0.057	0.005
29	HE0940–1050	101	3.05	2.64315	0.00005	0.218	0.007
30	HE0940–1050	101	3.05	2.66771	0.00005	0.641	0.006
31	HE0940–1050	101	3.05	2.82568	0.00005	0.679	0.011
32	HE0940–1050	101	3.05	2.82673	0.00005	1.629	0.013
33	HE0940–1050	101	3.05	2.83465	0.00005	1.621	0.007
34	HE0940–1050	101	3.05	2.86086	0.00005	0.085	0.007
35	HE0940–1050	101	3.05	2.91698	0.00005	0.346	0.007
36	HE0940–1050	101	3.05	2.93772	0.00005	0.133	0.009
37	HE0940–1050	101	3.05	3.03859	0.00005	0.091	0.006
38	PKS2126–158	138	2.43	2.32389	0.00027	4.056	0.106
39	PKS2126–158	138	2.43	2.40790	0.00017	0.543	0.003
40	PKS2126–158	130	2.58	2.23069	0.00010	5.385	0.085
41	PKS2126–158	131	2.90	2.14980	0.00005	0.092	0.012
42	PKS2126–158	131	2.90	2.16316	0.00005	3.748	0.031
43	PKS2126–158	131	2.90	2.35667	0.00005	0.474	0.035
44	PKS2126–158	131	2.90	2.43630	0.00005	0.250	0.020
45	PKS2126–158	131	2.90	2.82301	0.00005	0.376	0.023
46	PKS2126–158	131	2.90	2.84763	0.00005	0.653	0.025
47	PKS2126–158	134	3.27	2.39401	0.00005	1.662	0.003
48	PKS2126–158	134	3.27	2.45961	0.00005	0.317	0.003
49	PKS2126–158	134	3.27	2.48546	0.00005	0.086	0.003
50	PKS2126–158	134	3.27	2.55370	0.00005	0.162	0.003
51	PKS2126–158	134	3.27	2.63797	0.00005	2.277	0.003
52	PKS2126–158	134	3.27	2.67890	0.00005	0.695	0.003
53	PKS2126–158	134	3.27	2.72795	0.00005	0.371	0.004
54	PKS2126–158	134	3.27	2.76877	0.00005	3.366	0.006
55	PKS2126–158	134	3.27	2.81944	0.00005	0.590	0.006
56	PKS2126–158	134	3.27	2.90709	0.00005	0.543	0.004
57	PKS2126–158	134	3.27	2.96326	0.00005	0.314	0.004

Continued on Next Page...

Table C3 – Continued

#	Field	Quasar #	z_{qso}	z_{abs}	σz_{abs}	EW	σ EW
58	PKS2126–158	134	3.27	2.96748	0.00005	0.355	0.004
59	PKS2126–158	134	3.27	3.09869	0.00005	0.021	0.003
60	PKS2126–158	134	3.27	3.21649	0.00005	0.299	0.003
61	PKS2126–158	128	3.86	3.08476	0.00031	0.476	0.003
62	PKS2126–158	128	3.86	3.35438	0.00038	0.480	0.002
63	PKS2126–158	128	3.86	3.40139	0.00024	0.480	0.002
64	PKS2126–158	128	3.86	3.57767	0.00012	1.370	0.003
65	PKS2126–158	128	3.86	3.73041	0.00030	0.606	0.003
66	PKS2126–158	132	2.54	1.95150	0.00007	3.289	0.009
67	PKS2126–158	132	2.54	2.29910	0.00025	0.996	0.007
68	PKS2126–158	140	2.40	1.70540	0.00014	0.657	0.003
69	PKS2126–158	140	2.40	1.91800	0.00006	2.013	0.003
70	PKS2126–158	142	2.74	2.33881	0.00010	0.972	0.002
71	PKS2126–158	129	2.14	1.96477	0.00006	1.668	0.002
72	PKS2126–158	129	2.14	1.99582	0.00004	3.478	0.004
73	PKS2126–158	129	2.14	2.03533	0.00010	0.868	0.002
74	PKS2126–158	141	3.46	2.54500	0.00025	0.964	0.008
75	PKS2126–158	141	3.46	3.11388	0.00021	1.853	0.015
76	PKS2126–158	141	3.46	3.26671	0.00035	1.499	0.016
77	J0124+0044	53	2.30	1.89338	0.00023	0.690	0.009
78	J0124+0044	26	2.77	2.50922	0.00020	2.016	0.039
79	J0124+0044	26	2.77	2.76856	0.00024	1.140	0.008
80	J0124+0044	49	4.07	3.11067	0.00024	1.628	0.018
81	J0124+0044	68	2.38	1.88617	0.00025	1.045	0.039
82	J0124+0044	39	2.48	2.17616	0.00033	2.415	0.079
83	J0124+0044	59	2.59	2.51074	0.00025	2.154	0.131
84	J0124+0044	48	2.94	2.14277	0.00014	1.075	0.005
85	J0124+0044	48	2.94	2.63615	0.00020	2.203	0.061
86	J0124+0044	52	2.97	2.14105	0.00013	1.419	0.009
87	J0124+0044	52	2.97	2.67890	0.00034	3.328	0.146
88	J0124+0044	62	3.00	2.19593	0.00042	1.516	0.086
89	J0124+0044	21	2.50	2.45733	0.00027	1.784	0.109
90	J0124+0044	21	2.50	2.49697	0.00005	1.912	0.003
91	J0124+0044	47	2.54	2.15139	0.00010	1.189	0.004
92	J0124+0044	37	3.12	2.88094	0.00027	1.715	0.039
93	J0124+0044	24	3.42	3.34344	0.00051	0.911	0.028
94	J0124+0044	43	2.47	1.80487	0.00022	1.270	0.020
95	J0124+0044	64	2.64	2.54622	0.00040	2.785	0.315
96	J0124+0044	46	3.11	2.23941	0.00020	2.293	0.068
97	J0124+0044	60	3.81	2.83356	0.00005	0.877	0.013
98	J0124+0044	60	3.81	2.86629	0.00005	0.082	0.006
99	J0124+0044	60	3.81	2.91041	0.00005	0.701	0.014
100	J0124+0044	60	3.81	2.94202	0.00005	0.111	0.009
101	J0124+0044	60	3.81	2.98670	0.00005	1.943	0.019
102	J0124+0044	60	3.81	3.06528	0.00005	1.500	0.019
103	J0124+0044	60	3.81	3.14814	0.00005	0.115	0.019
104	J0124+0044	60	3.81	3.18796	0.00005	0.135	0.018
105	J0124+0044	60	3.81	3.39219	0.00005	1.186	0.023
106	J0124+0044	60	3.81	3.54813	0.00007	1.794	0.002
107	J0124+0044	60	3.81	3.67356	0.00004	2.420	0.001
108	J0124+0044	60	3.81	3.76553	0.00011	0.661	0.000
109	J0124+0044	40	2.53	2.39121	0.00021	2.372	0.058
110	J0124+0044	40	2.53	2.43175	0.00022	2.345	0.058
111	J0124+0044	67	2.38	2.26440	0.00031	1.211	0.041
112	J0124+0044	66	2.51	2.28225	0.00024	2.219	0.062
113	J0124+0044	66	2.51	2.47245	0.00022	1.335	0.017
114	J0124+0044	63	2.98	2.31409	0.00028	1.085	0.042

Continued on Next Page...

Table C3 – Continued

#	Field	Quasar #	z_{qso}	z_{abs}	σz_{abs}	EW	σ EW
115	J0124+0044	63	2.98	2.37429	0.00020	1.591	0.042
116	J0124+0044	63	2.98	2.47027	0.00028	1.155	0.039
117	J0124+0044	50	2.36	2.32717	0.00012	1.766	0.012
118	J1201+0116	122	3.36	2.43546	0.00006	3.754	0.007
119	J1201+0116	122	3.36	2.46989	0.00011	2.434	0.011
120	J1201+0116	122	3.36	3.26698	0.00015	2.168	0.016
121	J1201+0116	112	3.84	3.79466	0.00016	5.871	0.067
122	J1201+0116	104	2.38	1.65636	0.00008	2.675	0.017
123	J1201+0116	104	2.38	2.04113	0.00027	1.126	0.056
124	J1201+0116	108	3.52	3.42823	0.00039	8.836	0.666
125	J1201+0116	121	2.23	1.77878	0.00026	2.348	0.197
126	J1201+0116	110	3.20	2.37602	0.00005	0.101	0.006
127	J1201+0116	110	3.20	2.47715	0.00005	0.449	0.009
128	J1201+0116	110	3.20	2.68444	0.00005	1.451	0.022
129	J1201+0116	110	3.20	2.78999	0.00005	0.396	0.023
130	J1201+0116	110	3.20	3.07951	0.00010	0.734	0.032
131	Q0042–2627	5	3.29	2.47481	0.00005	0.998	0.031
132	Q0042–2627	5	3.29	2.50670	0.00005	0.281	0.052
133	Q0042–2627	5	3.29	2.72816	0.00005	0.421	0.037
134	Q0042–2627	5	3.29	2.77891	0.00005	0.108	0.035
135	Q0042–2627	5	3.29	2.82754	0.00005	0.288	0.037
136	Q0042–2627	5	3.29	3.10189	0.00005	0.538	0.039
137	Q0042–2627	5	3.29	3.14458	0.00005	0.389	0.071
138	Q0042–2627	5	3.29	3.21252	0.00005	0.272	0.065
139	Q0042–2627	5	3.29	3.23594	0.00010	0.843	0.003
140	Q0042–2627	7	2.79	2.33870	0.00010	0.620	0.130
141	Q0042–2627	7	2.79	2.34175	0.00007	6.356	0.050
142	Q0042–2627	7	2.79	2.59946	0.00009	1.145	0.007
143	Q0042–2627	12	2.90	2.49148	0.00017	1.475	0.019
144	Q0042–2627	12	2.90	2.82448	0.00009	1.256	0.012
145	Q0042–2627	14	3.05	2.26461	0.00009	1.037	0.008
146	Q0042–2627	14	3.05	2.33871	0.00008	0.619	0.004
147	Q0042–2627	14	3.05	2.56880	0.00010	0.800	0.140
148	Q0042–2627	14	3.05	2.73960	0.00010	1.410	0.250
149	Q0042–2627	14	3.05	2.75630	0.00010	0.730	0.180
150	Q0042–2627	8	2.48	2.14446	0.00012	1.905	0.035
151	Q0042–2627	9	2.46	1.75183	0.00006	0.734	0.002
152	Q0042–2627	9	2.46	1.86964	0.00006	2.220	0.027
153	Q0042–2627	9	2.46	2.02084	0.00007	0.818	0.006
154	Q0042–2627	9	2.46	2.15417	0.00023	0.514	0.009
155	Q0042–2627	9	2.46	2.27132	0.00005	1.710	0.019
156	Q0042–2627	9	2.46	2.43659	0.00003	1.127	0.003
157	Q0042–2627	9	2.46	2.43907	0.00004	0.946	0.003
158	Q0042–2627	1	3.33	2.49787	0.00011	0.561	0.006
159	Q0042–2627	1	3.33	2.90194	0.00006	1.212	0.004
160	Q0042–2627	1	3.33	3.24812	0.00011	0.691	0.012
161	Q0042–2627	1	3.33	3.25543	0.00012	0.755	0.005
162	Q0042–2627	16	3.44	2.71935	0.00005	0.202	0.015
163	Q0042–2627	16	3.44	2.81853	0.00005	2.061	0.038
164	Q0042–2627	16	3.44	3.04437	0.00005	3.086	0.024
165	Q0042–2627	16	3.44	3.12003	0.00005	0.882	0.014
166	Q0042–2627	16	3.44	3.12944	0.00005	0.402	0.017
167	Q0042–2627	16	3.44	3.15350	0.00005	0.180	0.020
168	Q0042–2627	16	3.44	3.25486	0.00005	1.255	0.016
169	Q0042–2627	16	3.44	3.37157	0.00005	0.453	0.016
170	Q0042–2627	6	2.50	1.88975	0.00011	1.213	0.012
171	Q0042–2627	6	2.50	1.95550	0.00010	0.710	0.080

Continued on Next Page...

Table C3 – Continued

#	Field	Quasar #	z_{qso}	z_{abs}	σz_{abs}	EW	σ EW
172	Q0042–2627	6	2.50	2.40002	0.00003	0.781	0.001
173	Q0042–2627	6	2.50	2.50560	0.00010	0.450	0.060
174	Q0042–2627	4	3.31	2.29549	0.00009	1.082	0.010
175	Q0042–2627	2	2.98	2.12850	0.00010	1.790	0.180
176	Q0042–2627	2	2.98	2.22710	0.00010	2.770	0.420

Table C3: C IV systems identified towards quasars in both our high and low resolution samples. The columns give the unique absorber number, the field for the absorber, the number from Table C1 of the quasar toward which the absorber was seen, the quasar’s redshift, the absorber redshift and one sigma error, and the observed EW in Å and one sigma error.